

A radio continuum and infrared study of Galactic H II regions

N. L. Martín-Hernández^{1,*}, J. M. van der Hulst¹, and A. G. G. M. Tielens^{1,2}

¹ Kapteyn Institute, PO Box 800, 9700 AV Groningen, The Netherlands

² SRON, National Institute for Space Research, PO Box 800, 9700 AV Groningen, The Netherlands

Received 12 July 2002 / Accepted 19 June 2003

Abstract. We present observations of the 4.8 and 8.6 GHz continuum emission towards 11 southern H II regions made with the Australian Telescope Compact Array. The observed objects were selected from the Infrared Space Observatory (ISO) spectral catalogue of compact H II regions (Peeters et al. 2002b). The morphologies observed for practically all the sources are consistent with them being ionized by a cluster of stars, rather than by a single star. The linear diameters of the regions range from 0.03 pc to 3 pc, the electron densities from 300 to $2.5 \times 10^4 \text{ cm}^{-3}$, and the Lyman continuum photon flux from 10^{47} to 10^{50} s^{-1} . We confirm the existence of a relation between the density and size of H II regions which can be fit by a power law shallower than that predicted by the classic Strömgren theory. The radio observations provide, in addition, information about the distribution of the ionized gas within the ISO apertures. As a result of the combined radio and infrared study, estimates of the extinction in the infrared and the metal content of the nebular gas were calculated. In this analysis, we also included several (ultra)compact H II regions previously observed by the Very Large Array. Values for extinction in the *K*-band between ~ 0 and 6 mag are found. The elemental abundances of nitrogen, neon, argon and sulphur were found to decrease with Galactocentric distance. Finally, the degree of ionization of the nebulae is confirmed to be correlated with the metal content.

Key words. instrumentation: interferometers – ISM: H II regions – radio continuum: ISM – ISM: abundances – ISM: dust, extinction

1. Introduction

H II regions are photoionized regions surrounding massive O and early B stars. When the O and B stars are newly formed, they are still deeply embedded in their parental molecular cloud and the associated H II regions are characterized by their small sizes (diameter ≤ 0.05 pc) and high densities ($n_e \gtrsim 10^4 \text{ cm}^{-3}$). These ultracompact H II regions evolve further into compact and classical H II regions when the dense, ionized gas expands into the surrounding molecular gas. Classical H II regions have diameters ≥ 0.5 pc and densities $\leq 10^3 \text{ cm}^{-3}$ (Garay & Lizano 1999). Dust in the molecular gas which surrounds the stars and their H II regions absorbs nearly all the stellar radiation, either directly or after being processed in the nebula, and re-emit it in the far-infrared. Because of the high degree of obscuration due to this surrounding dust, most H II regions are practically invisible at optical wavelengths and can only be studied at infrared and radio wavelengths.

Studies of large samples of ultracompact and compact H II regions have been made in the infrared using the IRAS LRS data (e.g. Simpson & Rubin 1990), ground-based observations with low resolution (e.g. Faison et al. 1998),

airborne observations with the Kuiper Airborne Observatory (e.g. Simpson et al. 1995; Afflerbach et al. 1997; Rudolph et al. 1997) and more recently, observations from space made with the Infrared Space Observatory (ISO) (e.g. Peeters et al. 2002b; Giveon et al. 2002b; Vermeij et al. 2002a). The ISO observations gave access, for the first time, to the complete 2.3–196 μm spectrum and allowed a study of the ionizing conditions in H II regions and derive their relative and absolute elemental abundances (e.g. Martín-Hernández et al. 2002a; Giveon et al. 2002b; Vermeij & van der Hulst 2002), and catalogue their molecular and dust content (Boogert 1999; Peeters et al. 2002a; Vermeij et al. 2002b).

Radio continuum surveys of ultracompact and compact H II regions with high angular resolution have been made with the Very Large Array (VLA) of the National Radio Astronomy Observatory (e.g. Wood & Churchwell 1989; Fich 1993; Garay et al. 1993; Kurtz et al. 1994; Afflerbach et al. 1996; Rudolph et al. 1996; Kurtz et al. 1999; Kim & Koo 2001). These observations have allowed systematic studies of the morphologies and physical conditions of H II regions (e.g. emission measure, physical size and electron density). There is, however, no equivalent radio study at high angular resolution of H II regions in the southern hemisphere. Such a study can be conducted with the Australian Telescope Compact Array (ATCA), located at the Paul Wild Observatory in Narrabri and part of the CSIRO Australia Telescope National Facility.

Send offprint requests to: N. L. Martín-Hernández,

e-mail: leticia.martin@obs.unige.ch

* Present address: Geneva Observatory, 1290 Sauverny, Switzerland.

Table 1. ATCA observations. Given are the IRAS name, the pointing coordinates, and the restoring beam and rms noise of the final image.

IRAS name	IRAS coordinates			Restoring beam				σ	
	RA (J2000.0)	Dec (J2000.0)		4.8 GHz θ ("×")	PA (°)	8.6 GHz θ ("×")	PA (°)	4.8 GHz (mJy/beam)	8.6 GHz (mJy/beam)
10589–6034	11 00 59.8	–60 50 27.1		1.87×1.72	–4.2	0.95×0.92	31.8	0.7	0.4
11143–6113	11 16 33.8	–61 29 59.4		1.74×1.47	–3.2	0.94×0.77	–1.7	0.2	0.1
12063–6259	12 09 01.1	–63 15 54.7		2.09×1.83	–5.2	1.19×0.94	–11.8	1.5	0.7
12073–6233	12 10 00.3	–62 49 56.5		1.91×1.63	–3.2	1.01×0.86	–5.3	3.7	2.1
12331–6134	12 36 01.9	–61 51 03.9		1.94×1.62	–4.0	1.02×0.83	–3.0	0.4	0.3
15384–5348	15 42 17.1	–53 58 31.5		1.93×1.53	–7.7	1.09×0.90	–11.0	0.3	0.2
15502–5302	15 54 06.0	–53 11 36.4		2.49×1.74	–21.0	1.44×0.94	–32.7	2.9	1.9
16128–5109	16 16 39.3	–51 16 58.3		2.12×1.45	–20.8	1.23×0.85	–29.7	1.0	0.8
17160–3707	17 19 26.1	–37 10 53.8		3.14×1.73	–4.0	1.43×0.83	–6.0	0.5	0.5
17221–3619	17 25 31.7	–36 21 53.5		3.38×1.67	–6.6	1.73×0.92	–9.5	0.6	0.1
17279–3350	17 31 18.0	–33 52 49.4		3.69×1.68	–5.6	1.92×0.93	–7.5	0.3	0.2

We have completed a survey of compact H II regions in the southern hemisphere with the ATCA at both 4.8 and 8.6 GHz. Our sample consists of 11 sources selected from the ISO spectral catalogue of compact H II regions (Peeters et al. 2002b). These source were among those located in the South Hemisphere for which radio interferometric observations were not available in the literature. These radio continuum observations provide us with an unobscured view of the morphology of these H II regions and estimates of several properties of the ionized gas such as the emission measure, the physical size and the electron density. Moreover, the radio fluxes can be used to give an indirect measure of the total number of ionizing photons, and hence, provide information on the nature and the number of ionizing stars in the H II regions.

These observations provide, in addition, information about the distribution of the ionized gas within the ISO apertures. This information ensures reliable comparison between the radio and the ISO observations. This multi-wavelength comparison allows us to estimate the extinction by contrasting the HI recombination line fluxes observed by ISO with the thermal radio fluxes, which measure the total ionized mass without any effects from extinction. Moreover, the use of the thermal radio fluxes in combination with the fine-structure lines in the ISO spectra allows us to estimate accurate elemental abundances.

In order to increase the statistical significance of our sample, we have included observations of several northern compact H II regions made by Wood & Churchwell (1989) and Kurtz et al. (1994) with the VLA. These observations are analyzed in the same way as the ATCA sample.

This paper is structured as follows. Section 2 describes the ATCA observations and the data reduction. A comparison with single dish observations is made. Section 3 presents contour maps of the H II regions and discusses the sources individually. The VLA data included in the posterior analysis is also described here. In Sect. 4, estimates of the physical properties of the ionized gas calculated from the thermal radio fluxes are given. Section 5 presents the combined analysis of the ISO and radio continuum observations. This analysis includes

estimates of the near- and mid-infrared extinction and the elemental abundances of nitrogen, neon, sulphur and argon. Finally, Sect. 6 discusses and summarizes the results of the paper.

2. Observations and data reduction

The objects were observed with the ATCA. The ATCA is an East-West synthesis instrument with 5 22-m antennas on a 6 km track. Five antennas are movable into configurations with baselines between 31 m and 6 km. The data were obtained in snapshot mode during two different runs on 8–9 April 2000 and 18–19 May 2000 in the 6 km (6D) and 1.5 km (1.5D) configurations. The sample objects and pointing coordinates are listed in Table 1. Each object was observed 5 times each observing run for 8 min, so for each object we have an effective integration time of 80 min covering 10 different hour angles, separated by about 18 degrees in hour angle.

The ATCA data were calibrated according to standard techniques using the MIRIAD software package described in *The Miriad User's Guide*¹ (see also Sault et al. 1995). ATCA calibrator sources close to the target sources were used to track the gains and phases of the individual antennas. The flux density scale was calibrated using observations of the compact extragalactic source PKS 1934–638 (the ATCA primary calibrator), for which values of 5.829 Jy at 4.8 GHz and 2.842 GHz Jy at 8.6 GHz were adopted for both runs. PKS 1934–638 has no detectable linear polarization and therefore can be used to solve for polarization leakages. The images were formed using the technique of multi-frequency synthesis and uniform weighting with pixel sizes of 0.3". These images, with a typical theoretical rms of ~ 0.2 mJy beam^{–1}, were deconvolved using the SDI CLEAN algorithm (Steer et al. 1984) and restored with the diffraction limited beams. Values for the rms noise of the final images are summarized in Table 1.

Every image was analysed in the following way. The peak flux densities and coordinates of the different components were determined using the task *maxfit* in MIRIAD. The integrated flux densities were obtained from integrating the images within

¹ <http://www.atnf.csiro.au/computing/software/miriad>

the 3σ contour using the task *ellint*. We estimate that the uncertainty in these integrated flux densities is no larger than 10%. Finally, the sizes were determined using the task *imfit* and fitting an elliptical disk. Peak coordinates, peak and integrated flux densities, and sizes are reported in Table 2. In the case of sources with multiple components, the peak coordinate, peak flux density, and whenever possible, integrated flux density and size, are given for every individual component as labelled in Fig. 2.

2.1. Extended emission

Interferometric observations are limited to angular scales smaller than $\theta = \lambda/(d - D/2)$, where d is the shortest baseline (77 m for our observations) and D is the diameter of a single antenna (22 m for the ATCA). This limits our ATCA data to angular scales smaller than $\theta \sim 3'$ and $2'$ respectively for the 4.8 and 8.6 GHz observations. It is quite clear from Fig. 2 that most of the 8.6 GHz images of the more extended and complex sources suffer from this problem.

In addition to the missing short spacing information, these observations are limited by the coarse sampling of the u, v plane. Each observation consists only of 10 cuts in the u, v plane separated by about 18 degrees in hour angle, rather than continuous 12 hour tracks. Complex brightness distributions are therefore difficult to reconstruct reliably, which affects the fidelity of the images. Since we are mainly interested in using this data to get values for the total flux and the flux within ISO aperture size subregions, this limitation is less severe than the lack of very short spacings.

A way to quantify how much extended emission we are missing is by comparing our total flux densities to single dish observations. For this purpose we use the 64-m Parkes Telescope observations by Caswell & Haynes (1987), who quoted 5 GHz flux densities towards all of our sources except IRAS 17160. Figure 1 shows that the ratio between the single dish and our 4.8 GHz ATCA observations is less than a factor of 2 for all the sources except for IRAS 10589, IRAS 15502 and IRAS 17279. We discuss these differences for each source individually in the next section. At 8.6 GHz, the ratio between single-dish and interferometric flux densities is expected to be larger.

3. Contour maps and description of sources

Contour maps of the radio continuum emission at 4.8 GHz and 8.6 GHz of the 11 IRAS sources observed are shown in Fig. 2. The smoother appearance of the 4.8 GHz maps is due to the lower angular resolution (approximately half the angular resolution of the higher frequency observations). The contour levels are specified in the figure caption. Overplotted on the 4.8 GHz maps we also show the 4 nominal apertures of the ISO Short Wavelength Spectrometer (SWS): $14'' \times 20''$, $14'' \times 27''$, $20'' \times 27''$ and $20'' \times 33''$.

3.1. Comments on individual sources

IRAS 10589–6034. Observed in the I -band ($0.8 \mu\text{m}$) as a nebula of approximately $20''$ (Persson & Campbell 1987) embedded in a larger diffuse extension, our ATCA maps reveal a compact cometary-like region of $14'' \times 12''$ (cf. Fig. 2 a) exhibiting a compact head towards the West and a tail trailing to the East. It was previously observed at radio frequencies with the Parkes Telescope, with a 6 cm flux density approximately six times larger than the one we measure (Caswell & Haynes 1987). IRAS 10589–6034 is the source which shows the largest difference with the single dish observations (cf. Fig. 1). We examined the 8.3 μm Midcourse Space Experiment (MSX) satellite observation of this object (the MSX observations are freely distributed by the MSX webpage via the NASA/IPAC Infrared Science Archive²). This image shows a large diffuse extension of approximately $3'$, which could account for the large difference between the ATCA and single dish measurements.

IRAS 11143–6113. This source has been previously observed at radio wavelengths using the Parkes Telescope (Caswell & Haynes 1987), with a measured flux density at 6 cm (3.1 Jy) in fair agreement with ours. The 4.8 GHz ATCA map (cf. Fig. 2b) shows a large, complex H II region of around $81'' \times 54''$ which contains multiple components, indicative of a cluster of embedded ionizing sources. The source presents sharp cut edges on the western and southern sides. The curious extension towards the North may reflect the expansion of the nebula into a less dense surrounding medium.

IRAS 12063–6259. This is a small and bright $H\alpha$ source (Russeil 1997). It has been previously mapped by the Parkes Telescope at 2 (Milne & Aller 1982) and 6 cm (Caswell & Haynes 1987). The 6 cm single-dish flux is 2400 mJy, only 1.2 times higher than our ATCA measurement. It has been classified as both an H II region and a planetary nebula (hence, its other designations He 2–77 and PK 298–00.1). However, the fact that it follows the color criteria defined by Wood & Churchwell (1989) and that it has an infrared luminosity ($4.5 \times 10^5 L_{\odot}$) and spectral content (Peeters et al. 2002b) typical of normal compact H II regions suggest that it is an H II region rather than a planetary nebula. Our ATCA observations (cf. Fig. 2c) show it to be a compact object of $16'' \times 7''$ embedded in a low brightness region of $28'' \times 25''$. The 4.8 GHz map shows two bright embedded components, A and B. The higher frequency map reveals the second component B to be formed by two smaller components B1 and B2. The existence of multiple components suggest that this region is ionized by a cluster of young stars rather than by a single star.

IRAS 12073–6233. $H\alpha$ observations (Russeil 1997) show it as a small source, likely located in the Carina arm. The ATCA maps (cf. Fig. 2d) reveal two main compact components, A and B, of $9'' \times 7''$ and $10'' \times 5''$, respectively, separated by $30''$, which lie in a large low brightness region. These two

² <http://irsa.ipac.caltech.edu/>

Table 2. ATCA results. Given are the peak coordinates, peak and integrated flux densities, and sizes.

Source	4.8 GHz					8.6 GHz				
	Component	Peak coordinates ^a (RA, Dec)	Peak ^b S_ν	Integ. ^{c, <} S_ν	Source ^d size	Comp.	Peak coordinates ^a (RA, Dec)	Peak ^b S_ν	Integ. ^{c, <} S_ν	Source ^d size
IRAS 10589		11:01:00.16 –60:50:22.4	79	1218	14 × 12		11:01:00.20 –60:50:22.2	24	1343	14 × 12
IRAS 11143		11:16:32.91 –61:30:12.7	6	2733	81 × 54 [‡]		★			
IRAS 12063				1961	28 × 25			1400		16 × 7
...	A	12:09:01.12 –63:15:52.9	158			A	12:09:01.04 –63:15:52.9	63		
...	B	12:09:01.01 –63:16:00.8	106			B1 [△]	12:09:00.99 –63:15:59.3	41		
						B2 [△]	12:09:01.17 –63:16:02.2	37		
IRAS 12073				15 377 [◇]					12 853 [◇]	
...	A	12:10:01.11 –62:49:53.9	383	4955	9 × 7	A	12:10:01.06 –62:49:53.6	184	4098	5.8
...	B	12:09:57.88 –62:49:33.5	141	1145	10 × 5	B	12:09:58.10 –62:49:32.8	57	656	4.5 × 1.8
IRAS 12331		12:36:01.23 –61:51:18.8	15	3528	73 × 62		12:36:01.28 –61:51:17.7	4	2699	68 × 52
IRAS 15384		15:42:16.86 –53:58:33.4	59	4753	44 × 37		15:42:16.87 –53:58:33.8	16	3505	31.5 × 26
IRAS 15502				2172					3202	
...	A	15:54:06.40 –53:11:40.2	555	1853	4.7	A	15:54:06.43 –53:11:40.6	543	3013	3.6
...	B	15:54:05.26 –53:11:39.4	90	234	2.5	B	▷			
IRAS 16128				9266 [◇]	22.5 × 14 [†]				5795	22.5 × 14 [†]
...	A	16:16:41.06 –51:17:02.0	182			A	16:16:41.06 –51:17:02.1	65		
...	B	16:16:40.55 –51:17:08.5	161			B	16:16:40.78 –51:17:09.2	45		
...	C	16:16:40.32 –51:17:13.1	155			C	16:16:40.44 –51:17:08.2	55		
...	D	16:16:40.25 –51:17:13.1	164			D	16:16:40.23 –51:17:13.0	74		
IRAS 17160				5475 [◇]						
...	A	17:19:27.51 –37:11:02.7	123	1230 [‡]	13 [†]	A	17:19:27.48 –37:11:04.6	41	2365	27 × 19
...	B	17:19:26.92 –37:10:24.6	49	110	4.4	B	17:19:27.01 –37:10:25.2	14	67	3.2
...	C	17:19:32.74 –37:10:46.8	53	200	10 × 5	C	17:19:32.76 –37:10:47.4	18	54	2.7
...	D	17:19:35.69 –37:10:56.5	142	213	3.1	D	17:19:35.68 –37:10:56.4	81	223	2.2
...	E	17:19:25.55 –37:10:04.6	4	5	< 2.3	E	17:19:25.60 –37:10:04.9	38	39	< 1.1
IRAS 17221		17:25:31.05 –36:21:51.9	19	2905	67		17:25:31.01 –36:21:52.1	5	1479	44
IRAS 17279				1532 [◇]						
...	A	17:31:17.62 –33:52:45.4	24		16 × 11 [†]	A	17:31:17.63 –33:52:45.1	10	517	20 [†]
...	B	17:31:20.54 –33:53:25.7	95	103	2.7	B	17:31:20.54 –33:53:25.7	46	62	1.9
...	C	17:31:15.04 –33:51:16.0	85	124	3.4	C	17:31:15.03 –33:51:15.8	47	113	2.0

^a Coordinates in right ascension and declination (J2000.0); the units of right ascension are hours, minutes and seconds; the units of declination are degrees, arcmin and arcsec.^b Peak flux density in mJy beam⁻¹. ^c Total integrated flux density in mJy. ^d Source size in arcsec. [‡] The structure on the north extends up to 40". * Not properly reconstructed.[△] The component B observed at 4.8 GHz is decomposed in two components (B1 and B2) by the 8.6 GHz observation. [▷] Weak component. [†] Core size. [‡] Core flux density.[◇] Emission integrated over the whole field. (<) Uncertainty is not larger than 10%.

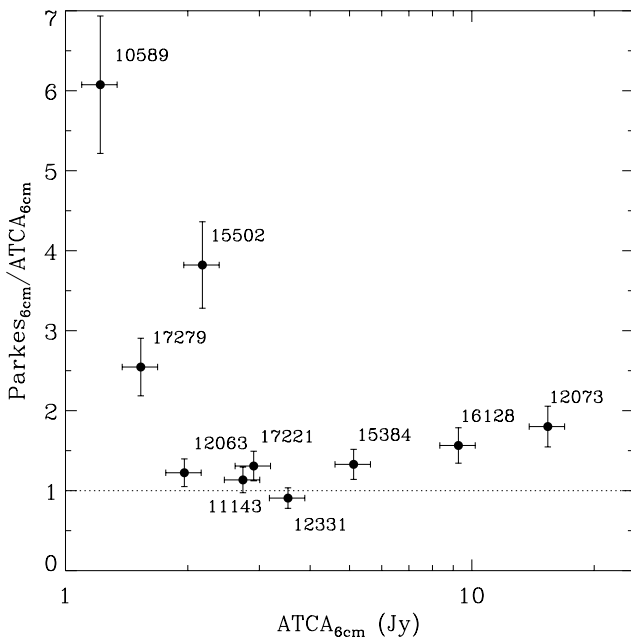


Fig. 1. Comparison between the total 6 cm flux densities measured from the ATCA and the single dish observations made with the Parkes Telescope (Caswell & Haynes 1987). A 10% uncertainty is considered for both ATCA and Parkes flux densities.

components coincide with the two bright, compact sources observed in the Bry line by Bik et al. (2003, in prep.). Component A shows a core-halo morphology. The arc-like shape of component B is also present in the Bry image. The single dish observations made with the Parkes Telescope measured a total flux density of 27.7 Jy at 6 cm (Caswell & Haynes 1987), 1.8 times higher than the total ATCA flux density.

IRAS 12331–6134. This source appears in our ATCA maps (cf. Fig. 2e) as a quasi-spherical and multi-peaked object with a diameter of approximately 67". The brightest peaks are located on the South. The total flux density contained in our 4.8 GHz map, 3.5 Jy, is in very good agreement with the flux density of 3.2 Jy measured by the Parkes Telescope (Caswell & Haynes 1987).

IRAS 15384–5348. Previous single dish observations at 6 cm (Caswell & Haynes 1987) give a flux density of 6.8 Jy for this object, while we obtain a total flux density of 5.1 Jy. The 4.8 GHz map (cf. Fig. 2f) reveals a cometary-like source exhibiting a compact core of 21" × 11" size – which contains 50% of the total flux density –, and a tail trailing to the East. An unidentified linear structure appears on the West side of the H II region, extending up to approximately 50". The 8.6 GHz map shows only the compact core and resolves out both the low brightness tail and the linear structure. A detailed analysis of this linear structure and its possible nature is given in Sect. 3.2.

IRAS 15502–5302. The 4.8 GHz (cf. Fig. 2g) shows two compact objects, A and B, of 4.7" and 2.5", respectively, and separated by 9". Component A has a peak flux 6 times higher than component B. The 8.6 GHz map shows clearly component A. Both A and B coincide in position and size with two bright objects observed in Bry by Bik et al. (2003, in prep.). The Parkes Telescope observation at 6 cm gives a total flux density of 8.3 Jy (Caswell & Haynes 1987), approximately 4 times higher than our 6 cm value. This larger single dish flux density probably reflects extended emission missed by the ATCA. Examination of the Bry image indeed reveals low luminosity structures spread over a region of approximately 1' around IRAS 15502.

IRAS 16128–5109. This source is classified by the SIMBAD Astronomical Database³ as a possible planetary nebula, hence its denomination PK 332–00.1. Both ATCA 4.8 and 8.6 GHz maps (cf. Fig. 2h) reveal a similar morphology for this source. The 4.8 GHz map shows a compact object of 22" × 14" embedded in a low brightness region which extends approximately 2' in the South-East North-West direction. The maps reveal 4 embedded cores (A, B, C and D). Two arm-like structures, one heading to the North-West and the other to the South-East, are apparent in both maps. The curved shape traced by the compact embedded cores is also evident in the Bry image by Bik et al. (2003, in prep.). Previous observations at 6 cm with the Parkes Telescope (Caswell & Haynes 1987) give a total flux density of 14.5 Jy, in contrast with the flux density of 9.3 Jy that we measure.

IRAS 17160–3703. This source appears in our ATCA maps (cf. Fig. 2i) as a complex source which spreads over a region of approximately 2.5'. The source is poorly imaged because its extent is too large in comparison with the restoring beam of the observations. We distinguish a main complex, component A, which at 4.8 GHz is characterized by a double core of approximately 13" and a flux density of 1.2 Jy. At 8.6 GHz, most of the diffuse emission observed at the lower frequency is resolved out, and component A appears as a source of 28" × 18" with a total flux density of 2.4 Jy. Component B is a compact object located to the North of A, at a distance of approximately 40", and likely connected to A. The connection of components C, D and E to A is not evident from the maps, but we will assume that they are at the same location as A. Component C appears in the 4.8 GHz map as a cometary source of 10" × 5" with a flux density of ~110 mJy, and located at ~1' to the East of component A. At 8.6 GHz, only the core, which has a semi-arc appearance, is observed. Component D, located at ~1.6' also to the East of component A, is a strong and resolved compact object at both frequencies. Component E, an unresolved compact object of less than 1.1", is located ~1' to the North of A. The nature of components D and E is not clear. Our data suggest that they have thermal spectral with indices of 0.08 and 3.52 respectively. The examination

³ <http://cdsweb.u-strasbg.fr/Simbad.html>

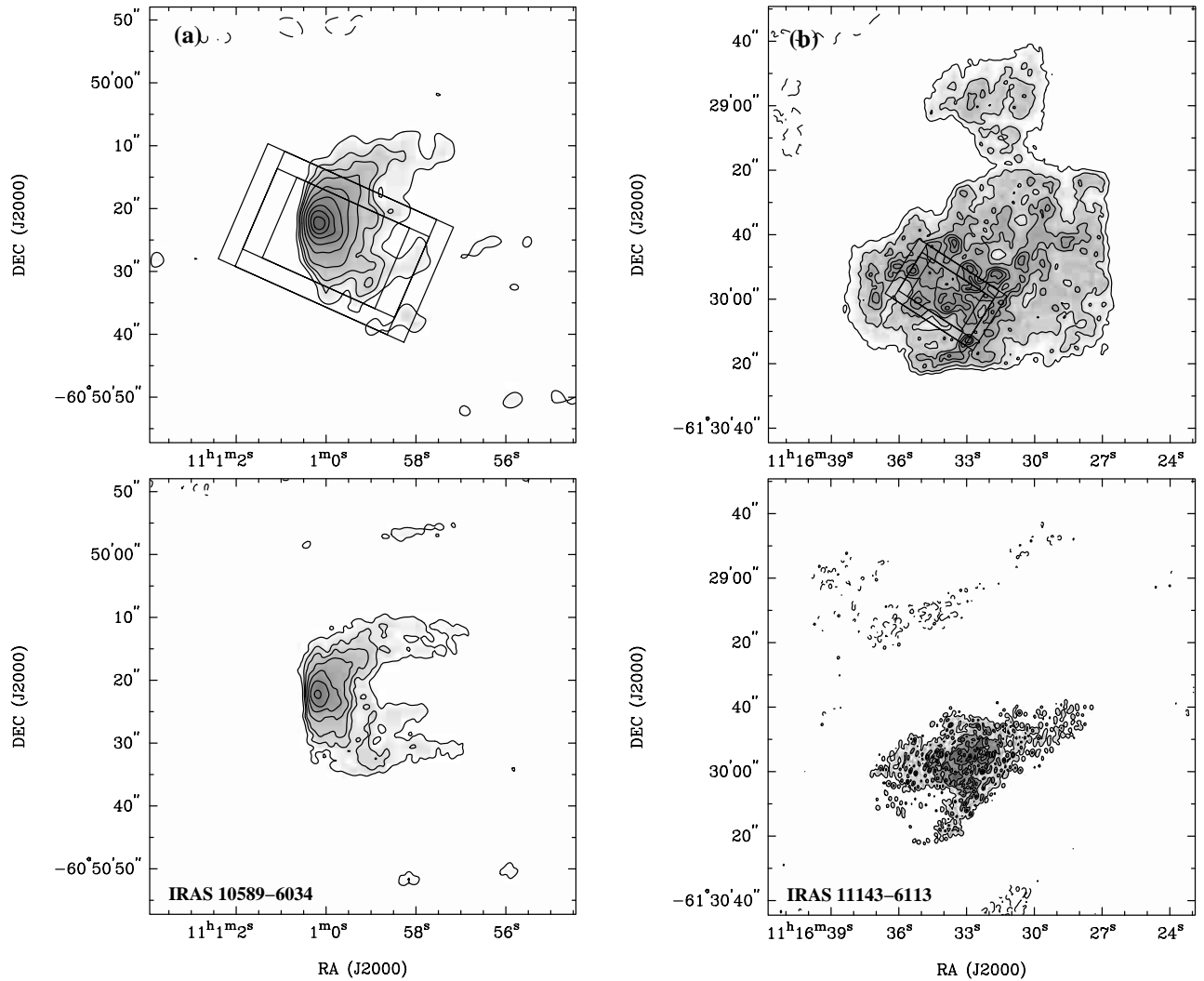


Fig. 2. **a)** 4.8 (top) and 8.6 GHz (bottom) maps of IRAS 10589–6034. Contour levels are (top) $-3, -1, 3, 6, 9, 15, 25, 40, 60, 800$ and 100 times the image rms $\sigma = 0.7 \text{ mJy beam}^{-1}$ and (bottom) $-3, 3, 6, 9, 15, 25, 40$ and 60 times the image rms $\sigma = 0.4 \text{ mJy beam}^{-1}$. **b)** 4.8 (top) and 8.6 GHz (bottom) maps of IRAS 11143–6113. Contour levels are (top) $-3, 3, 6, 12, 18, 24$ and 30 times the image rms $\sigma = 0.2 \text{ mJy beam}^{-1}$ and (bottom) $-3, 3, 9, 15, 25$ and 35 times the image rms $\sigma = 0.1 \text{ mJy beam}^{-1}$. The 4 nominal ISO-SWS beams are plotted on top of the 4.8 GHz maps.

of the *SuperCOSMOS Sky Survey* (SSS)⁴ image revealed no optical counterparts. Components A, B, C, D and E coincide with the objects GPSR5 350.103+0.082, 350.111+0.088, 350.118+0.070, 350.121+0.060 and 350.113+0.095 observed by Becker et al. (1994) as part of a 5 GHz survey of the Galactic Plane. They quote, respectively, total flux densities of 1300, 98, 145, 208 and 29 mJy.

IRAS 17221–3619. The 4.8 GHz ATCA map (cf. Fig. 2j) shows a quasi-spherical, complex source of $67''$ with a total flux density of 2.9 Jy, in contrast to the 3.8 Jy measured by the Parkes Telescope (Caswell & Haynes 1987). The brightest peaks are located on the South-West side of the nebula. Low brightness emission, which is resolved out by the 8.6 GHz observation, is seen on the North-East side.

IRAS 17279–3350. The source is poorly imaged because its extent is too large in comparison with the restoring beam of the observations. The 4.8 GHz map (cf. Fig. 2k) reveals a main complex component, A, formed by a core of $16'' \times 11''$ embedded in a large, low brightness region which spreads over $\sim 3.5'$ in the North-South direction. Most of this diffuse region is resolved out by the 8.6 GHz observation, where only a $20''$ region around the core and some residual emission on the South-East remain. Two compact objects of less than $2''$, B and C, are also observed. Component B is located at $54''$ to the South-East of A, while C is located at $1.6'$ to the North-West of A. These two objects were previously observed at 5 GHz by Becker et al. (1994) (GPSR5 354.185–0.074 and 354.205–0.039), who measure flux densities of 71 and 73 mJy, respectively. The nature of sources B and C is unclear. Our data suggest that the sources are slightly resolved and have non-thermal spectra with indices of -0.87 and -0.16 respectively. They could be ultracompact H II regions, pulsars, planetary nebulae

⁴ <http://www-wfau.roe.ac.uk/sss/index.html>

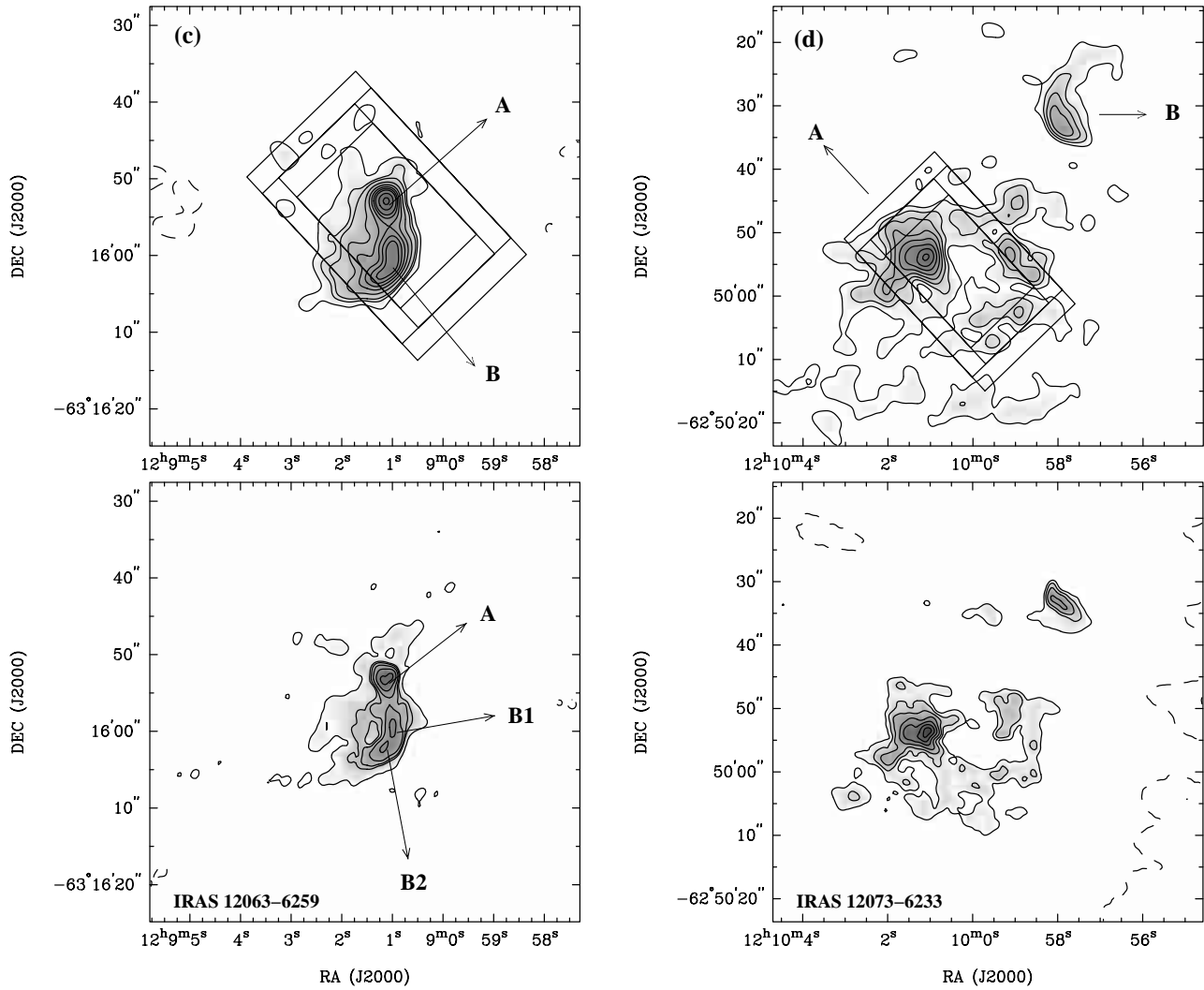


Fig. 2. continued. **c)** 4.8 (top) and 8.6 GHz (bottom) maps of IRAS 12063–6259. Contour levels are (top) $-3, -1, 5, 9, 12, 20, 30, 40, 50, 60, 80$ and 100 times the image rms $\sigma = 1.5 \text{ mJy beam}^{-1}$ and (bottom) $-3, -1, 5, 9, 15, 20, 30, 50$ and 80 times the image rms $\sigma = 0.7 \text{ mJy beam}^{-1}$. **d)** 4.8 (top) and 8.6 GHz (bottom) maps of IRAS 12073–6233. Contour levels are (top) $-3, -1, 5, 9, 15, 25, 40, 60, 80$ and 100 times the image rms $\sigma = 3.7 \text{ mJy beam}^{-1}$ and (bottom) $-3, -1, 5, 9, 15, 25, 40, 60$ and 80 times the image rms $\sigma = 2.1 \text{ mJy beam}^{-1}$. The 4 nominal ISO-SWS beams are plotted on top of the 4.8 GHz maps.

or extragalactic background sources. No optical counterpart is found via the examination of the SSS image. The 6 cm flux density measured towards this object by Caswell & Haynes (1987) with the Parkes Telescope is 2.5 times larger than the one we quote here.

3.2. The linear feature in IRAS 15384–5348

A puzzling linear feature is seen on the western side of IRAS 15384–5348. This feature is oriented East-West and is approximately $55''$ in length and $15''$ in width. The feature is only observed at 4.8 GHz (cf. Fig. 2f). Since this feature is not detected in our 8.6 GHz image one would tend to conclude its emission is non-thermal with a very steep spectral index. On the other hand, the faint emission at the eastern side of the H II region, which is at about the same level of brightness, is not seen either in the 8.6 GHz image. This suggests that the factor 1.6 difference in the length of the shortest spacing, coupled

to the extent of the emission in this H II region, severely hampers a direct comparison. It certainly makes a direct estimate of the spectral index of the extended emission impossible. We conducted a test to check whether the short spacing problem is causing the disappearance of the linear feature at 8.6 GHz. We created a 4.8 GHz image with the same spacings as the 8.6 GHz image by eliminating all spacings shorter than the equivalent shortest spacing (in $k\lambda$) at 8.6 GHz. In the new 4.8 GHz image, only the compact core of the H II region is present. This indicates that the absence of the filament in the 8.6 GHz image is indeed a short spacing problem.

Figure 3 (left) shows the 4.8 GHz continuum contours overlaid on the SSS *I*-band image. Five radio knots can be distinguished along the filament which we will label 1 to 5 from East to West respectively. Knot 3 is the brightest one, with a peak flux density of $5.4 \text{ mJy beam}^{-1}$. The knot structure is highly symmetric with respect to knot 3. Knots 2 and 4 are separated from knot 3 by $8.6''$; knots 1 and 5, on the other hand, are also

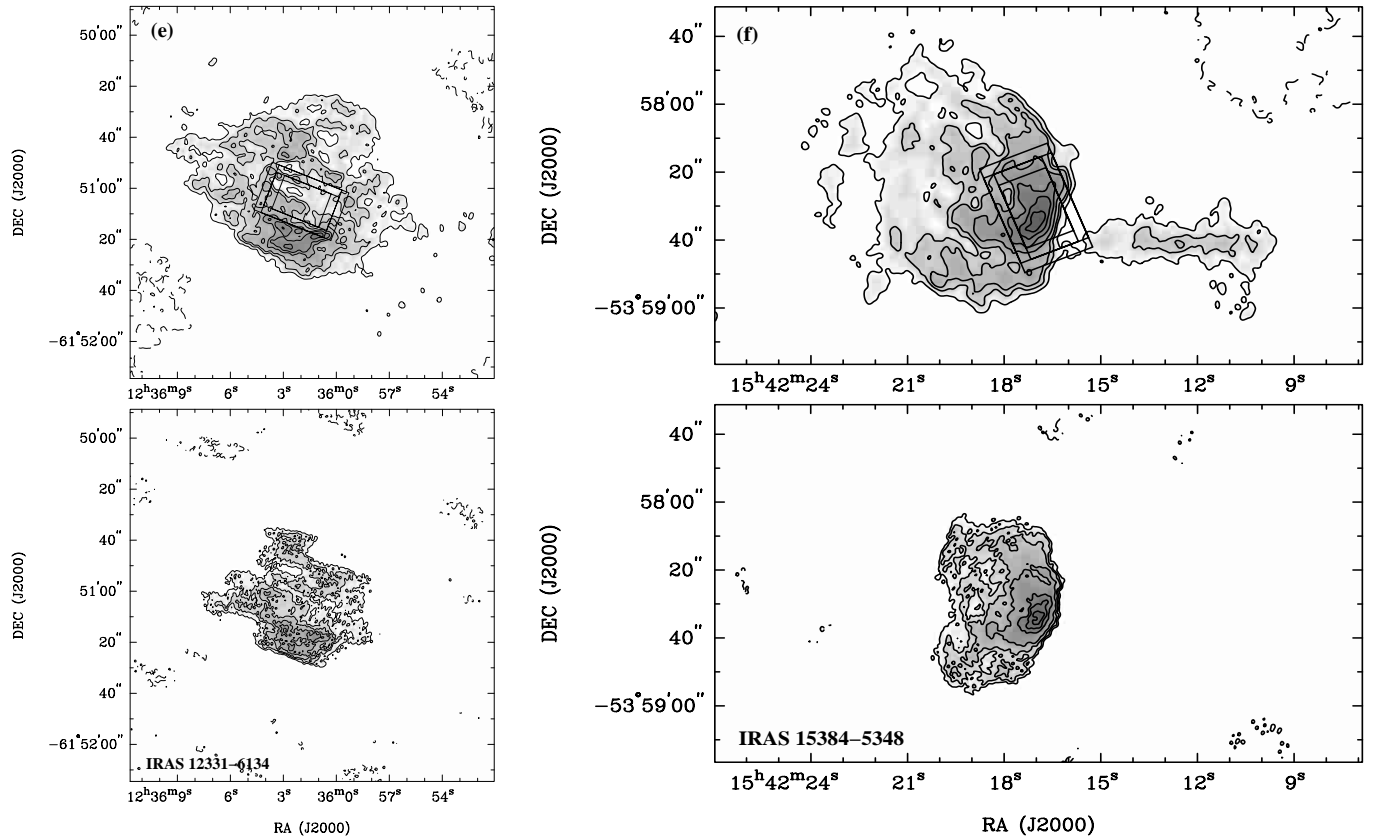


Fig. 2. continued. **e)** 4.8 (top) and 8.6 GHz (bottom) maps of IRAS 12331–6134. Contour levels are (top) $-3, -1, 3, 6, 9, 15, 20$ and 28 times the image rms $\sigma = 0.4 \text{ mJy beam}^{-1}$ and (bottom) $-3, 3, 4.5, 6, 8$ and 10 times the image rms $\sigma = 0.3 \text{ mJy beam}^{-1}$. **f)** 4.8 (top) and 8.6 GHz (bottom) maps of IRAS 15384–5348. Contour levels are (top) $-3, -1, 3, 9, 15, 30, 60, 100$ and 150 times the image rms $\sigma = 0.4 \text{ mJy beam}^{-1}$ and (bottom) $-3, 3, 6, 10, 20, 40, 60$ and 80 times the image rms $\sigma = 0.2 \text{ mJy beam}^{-1}$. The 4 nominal ISO-SWS beams are plotted on top of the 4.8 GHz maps.

symmetrically located from knot 3 ($19.7''$). As well, the peak flux densities of knots 2 and 4 agree ($4.4 \text{ mJy beam}^{-1}$). Knots 1 and 5 are weaker (2.7 and $3.6 \text{ mJy beam}^{-1}$). This suggests the possibility that we have detected an extragalactic radio source, though the filament does not really resemble the classic double radio lobe structure.

On the SSS, only two faint stars ($I \sim 17 \text{ mag}$) are coincident with the radio feature. They are located, however, at $4.6''$ to the North-West and $7.0''$ to the South-West of knot 3 and it is therefore unlikely that they are directly connected to the radio knot. The lack of a clear optical counterpart is, on the other hand, not surprising because of the large extinction in this direction. The H II region IRAS 15384–5348, for instance, suffers a visible extinction of $\sim 14 \text{ mag}$ (Sect. 5.1).

We also looked at images in the mid-infrared. Here we find a striking resemblance. Figure 3 (right) shows the $4'$ field of view around the objects observed by the MSX satellite at $8.3 \mu\text{m}$. Overlaid on the MSX image are the contours of the 4.8 GHz continuum smoothed to a resolution of $20''$, equivalent to that of the MSX. While the radio continuum image delineates the ionized gas (and possibly non-thermal emission), the $8.3 \mu\text{m}$ image includes the dominant PAH molecular emission at $6.2, 7.7$ and $8.7 \mu\text{m}$, which is particularly strong in the neutral zone (PDR) surrounding the ionized gas. The mid-infrared image is rather complex, with extensions at both the

eastern and western sides of the H II region. The large extension to the western side appears to coincide with the radio feature. Since radio galaxies seldom show bright infrared emission associated with their radio lobes, this points towards a Galactic origin for the filament, and perhaps this structure represents an embedded protostar with an associated jet.

3.3. VLA data

Similar high-resolution radio continuum observations of “northern” ultracompact H II regions have been made using the VLA of the National Radio Astronomy Observatory. 15 sources out of our ISO sample (Peeters et al. 2002b) had been observed in the surveys by Wood & Churchwell (1989) and Kurtz et al. (1994) at either 4.9 or 8.4 GHz. The images resulting from these observations were kindly provided to us by Ed Churchwell.

Eight out of these 15 sources were disregarded for various reasons: (i) no strong infrared lines have been detected with ISO (IRAS 02575+6017 and IRAS 18162–2048); (ii) the ISO-SWS apertures completely missed the H II region as outlined by the radio continuum emission (IRAS 21306+5540); (iii) the $\text{Br}\alpha$ line flux predicted using the integrated radio flux density in the SWS aperture where this line is

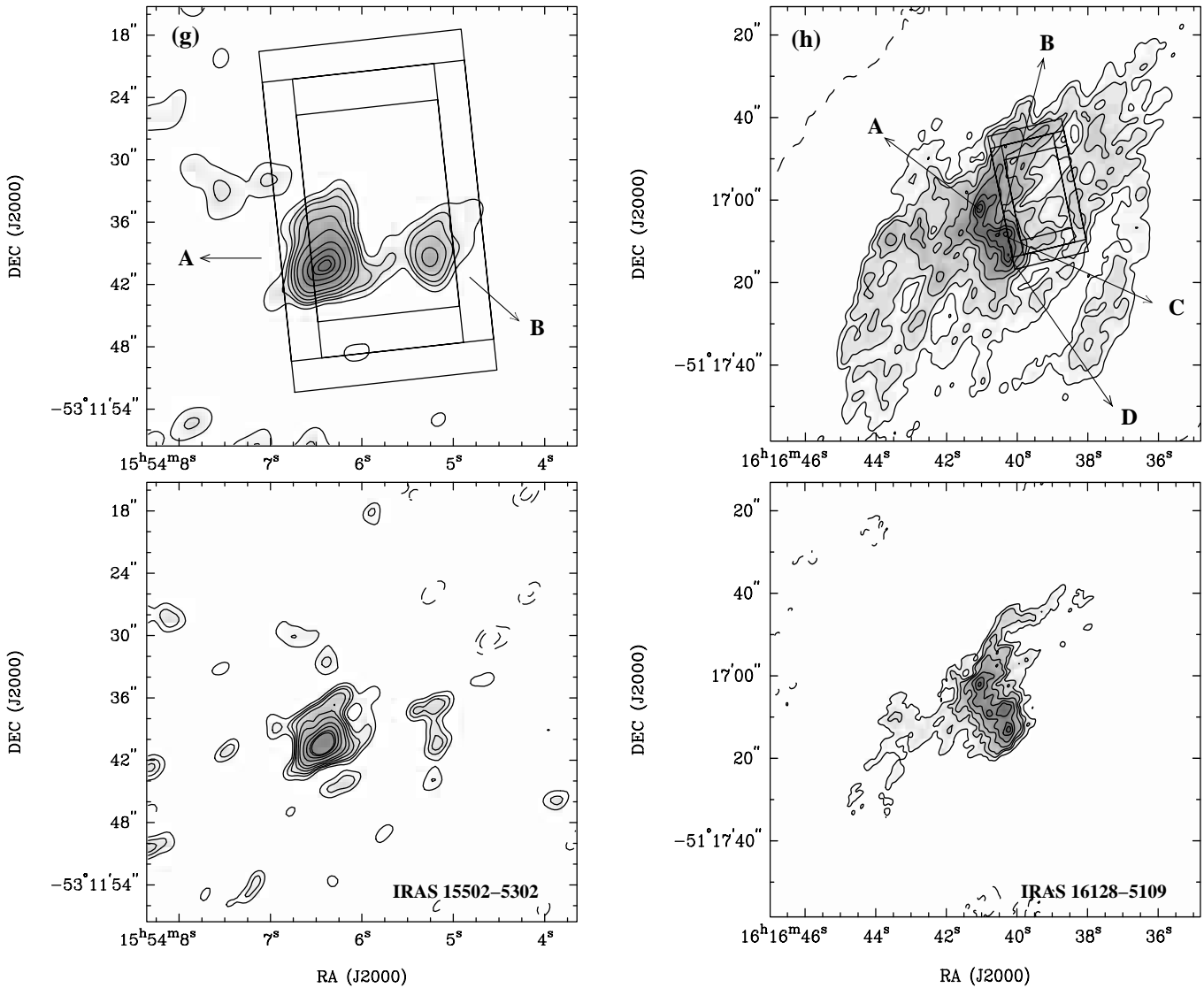


Fig. 2. continued. **g**) 4.8 (top) and 8.6 GHz (bottom) maps of IRAS 15502–5302. Contour levels are (top) –3, –1, 3, 9, 15, 25, 40, 80, 120, 160 and 180 times the image rms $\sigma = 2.9$ mJy beam $^{-1}$ and (bottom) –3, –1, 3, 9, 20, 40, 80, 140, 200 and 260 times the image rms $\sigma = 1.9$ mJy beam $^{-1}$. **h**) 4.8 (top) and 8.6 GHz (bottom) maps of IRAS 16128–5109. Contour levels are (top) –3, –1, 3, 9, 20, 50, 100, 150, 200 and 250 times the image rms $\sigma = 0.7$ mJy beam $^{-1}$ and (bottom) –3, 3, 6, 9, 15, 30, 50 and 80 times the image rms $\sigma = 0.8$ mJy beam $^{-1}$. The 4 nominal ISO-SWS beams are plotted on top of the 4.8 GHz maps.

observed is smaller than the observed line flux by ISO-SWS (IRAS 18434–0242, IRAS 18469–0132, IRAS 18502+0051, IRAS 22308+5812 and IRAS 23030+5958).

The remaining seven sources are listed in Table 3, where the wavelength of the observation, the rms noise, the total integrated flux density and the size are given. Contour maps with the 4 nominal ISO-SWS apertures are presented in Fig. 4. The Galactocentric and heliocentric distances to these sources (Peeters et al. 2002b) are listed in Cols. 2 and 3 of Table 4.

4. Physical properties of the ionized gas

It is clear from our continuum images that many sources have complex structures. Complicated geometries hamper the determination of important physical parameters such as opacity, electron density and emission measure because the geometry of

the source is required. The simplest geometry one can consider is a spherical, homogeneous H II region. In view of the radio contour maps, most of the sources are *not* spheres. However, we can estimate approximate physical properties by considering the objects to be spheres with a total flux density and diameter equal to the ones reported in Table 2. This approximation is appropriate for the quasi-spherical and point sources such as IRAS 12073 A, IRAS 15502 A and B, IRAS 17160 B, D and E or IRAS 17279 B and C. In the case of the other, more complex sources, the geometrical average of the major and minor axes can be taken as a representative size. The cases of IRAS 16128, IRAS 17160 A and IRAS 17279 A are more complicated. They are, however, better resolved by the 8.6 GHz observations, and the corresponding flux densities and sizes are used instead to characterize the physical properties of the compact cores.

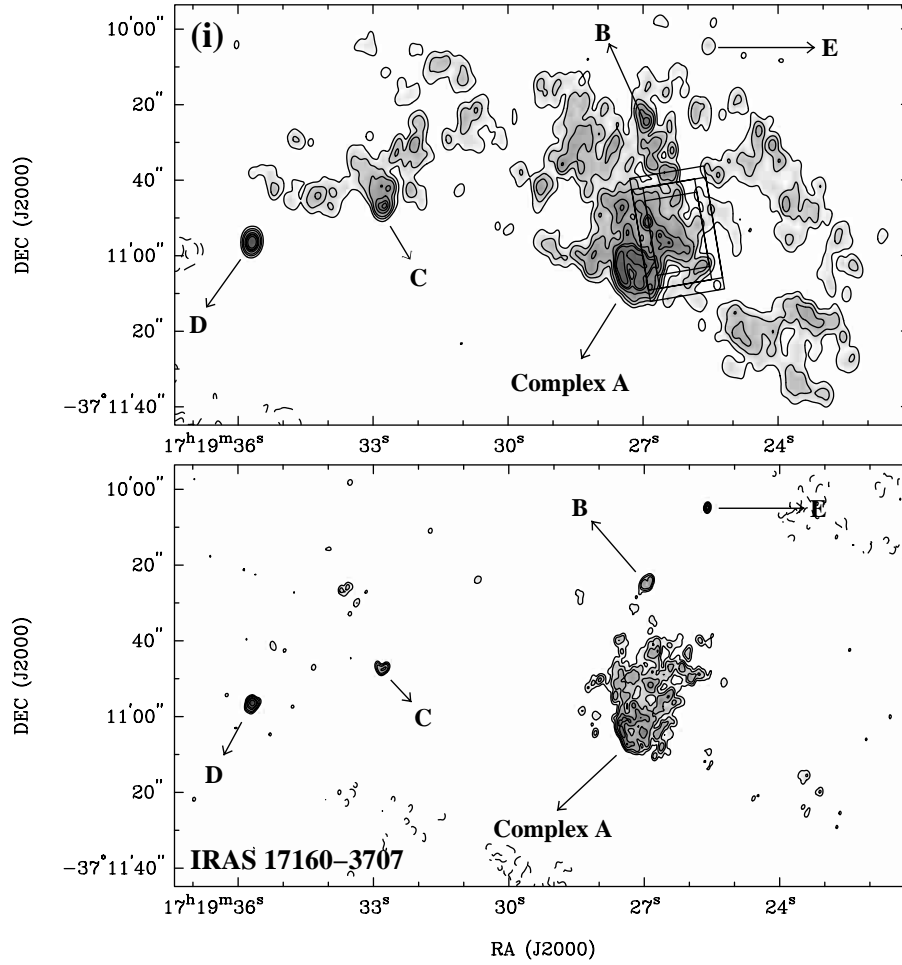


Fig. 2. continued. **i):** 4.8 (top) and 8.6 GHz (bottom) maps of IRAS 17160–3707. Contour levels are (top) –3, –1, 3, 9, 20, 50, 80, 100 and 150 times the image rms $\sigma = 0.5 \text{ mJy beam}^{-1}$ and (bottom) –3, 3, 6, 12, 30, 50 and 100 times the image rms $\sigma = 0.5 \text{ mJy beam}^{-1}$. The 4 nominal ISO SWS beams are plotted on top of the 4.8 GHz map.

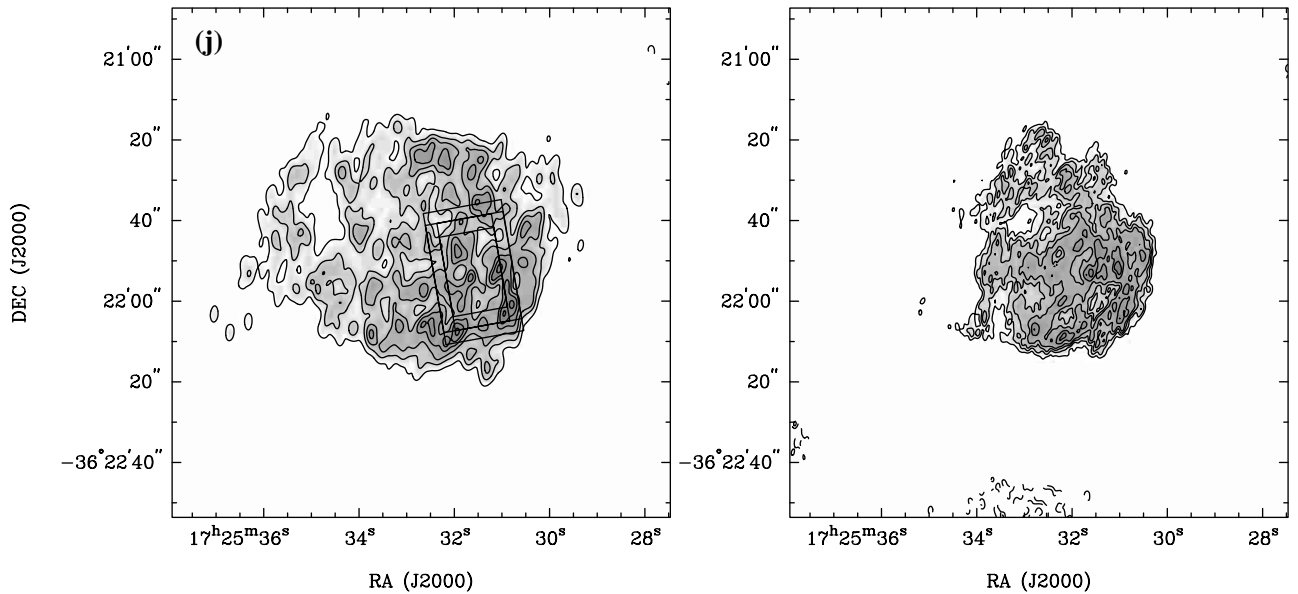


Fig. 2. continued. **j)** 4.8 (left) and 8.6 GHz (right) maps of IRAS 17221–3619. Contour levels are (left) –3, –1, 3, 6, 10, 15, 20 and 26 times the image rms $\sigma = 0.6 \text{ mJy beam}^{-1}$ and (right) –3, 3, 6, 10, 15, 25 and 35 times the image rms $\sigma = 0.1 \text{ mJy beam}^{-1}$. The 4 nominal ISO SWS beams are plotted on top of the 4.8 GHz map.

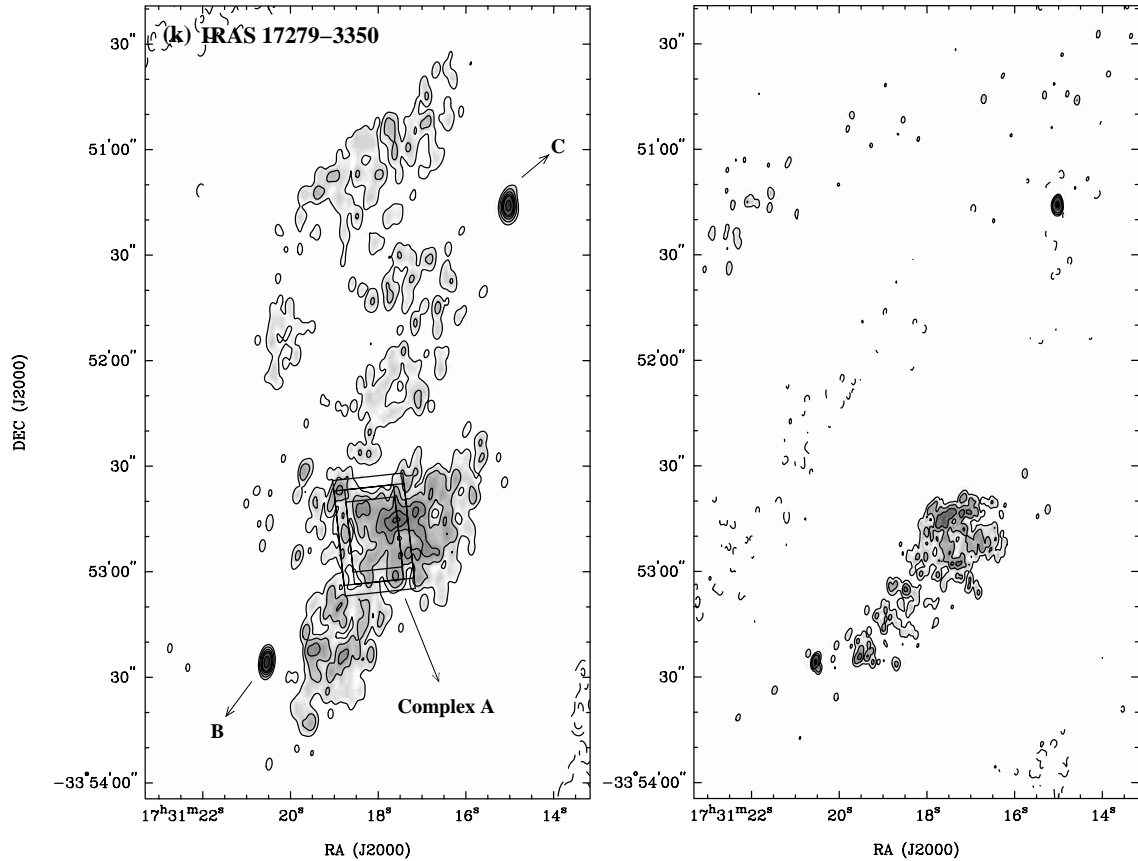


Fig. 2. continued. **k**) 4.8 (left) and 8.6 GHz (right) maps of IRAS 17279–3350. Contour levels are (left) $-3, -1, 3, 9, 25, 50, 80$ and 200 times the image rms $\sigma = 0.3 \text{ mJy beam}^{-1}$ and (right) $-3, 3, 9, 25$ and 100 times the image rms $\sigma = 0.2 \text{ mJy beam}^{-1}$. The 4 nominal ISO SWS beams are plotted on top of the 4.8 GHz map.

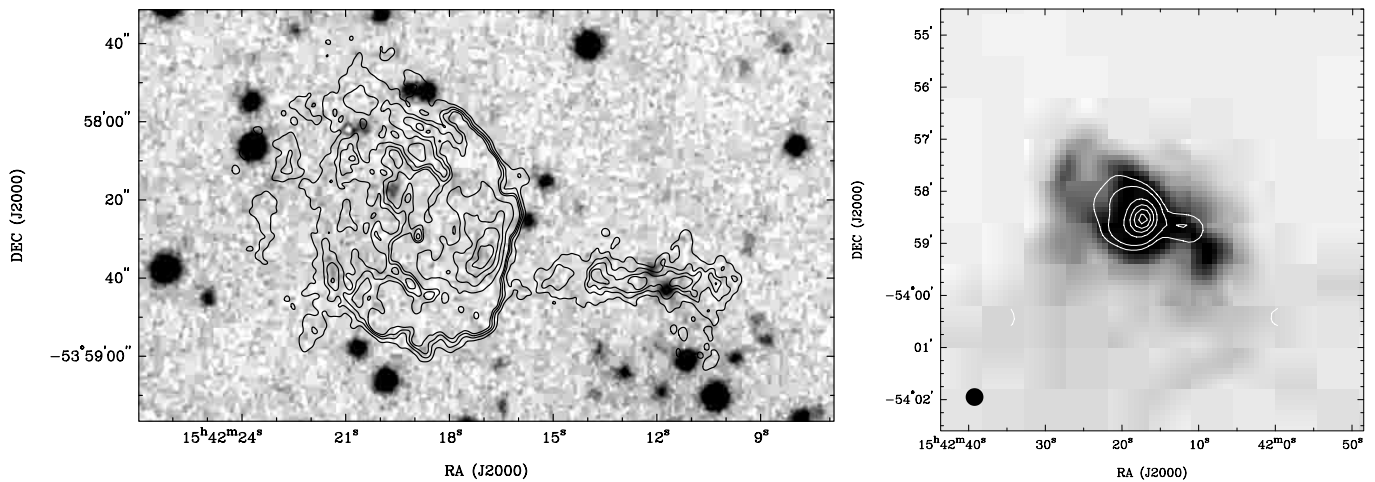


Fig. 3. *Left:* SuperCOSMOS Sky Survey image in the *I*-band of IRAS 15384–5348. The 4.8 GHz continuum contours are overlaid at values of $3, 6, 9, 12, 30, 60, 100, 150$ times the image rms $\sigma = 0.2 \text{ mJy beam}^{-1}$. *Right:* MSX image of IRAS 15384–5348 at $8.3 \mu\text{m}$. Overlaid in white are the contours of the 4.8 GHz continuum smoothed to a resolution of $20''$ (beam is in the bottom left corner), equivalent to that of the MSX. The values of the contours are $5, 10, 30, 50, 70$ and 90% the peak flux density.

Another crucial factor in the determination of physical parameters, such as the physical diameter of the source and the Lyman continuum photon flux, is the distance to the object. Kinematic distances to the H II regions have been presented in Peeters et al. (2002b). The Galactic and heliocentric

distances towards the objects are given in Cols. 2 and 3 of Table 4. In the cases of IRAS 16128, IRAS 17160, IRAS 17221 and IRAS 17279, for which the heliocentric ambiguity has not been resolved, both the near and far distances are quoted. For these objects, two different linear sizes, electron densities and

Table 3. Results corresponding to the VLA data. Given are the source name, the frequency of the observation, the rms noise of the image, the integrated flux density and the source size.

Source	ν (GHz)	σ (mJy/beam)	Integ. S_ν (Jy)	Size ($''$)
IRAS 01045+6505	8.4	0.29	242	4.7
IRAS 18032–2032	8.4	1.24	461, 71, 66 [‡]	19 × 10, 4, 1 [‡]
IRAS 18479–0005	8.4	1.30	2588 [*]	4.8, 1.5 [‡]
IRAS 19442+2427	8.4	0.19	80 [†]	1, 12 × 7 [◇]
IRAS 19598+3324	8.4	2.57	3380	6
DR21	8.4	2.75	561, 864 [◁]	4.4 × 3, 6 × 3.2 [△]
IRAS 23133+6050	8.4	0.74	737	9

[†] Respective flux densities of components B, C and D. [‡] Respective sizes of components B, C and D. ^{*} The two main components A and B have flux densities of approximately 1315 and 571 mJy, respectively. [‡] Respective sizes of components A and B. [†] The compact core has a flux density of 32 mJy. [◇] Sizes of the compact and diffuse components, respectively. [◁] Flux densities of components A and B, respectively. [△] Sizes of components A and B, respectively.

Lyman continuum fluxes result because of this ambiguity in the distance. However, for the discussion in this paper we will only consider the near distance.

Considering an ionized, optically thin gas with an electron temperature T_e , the optical depth, τ_ν , is defined by:

$$\tau_\nu = T_b(\nu)/T_e, \quad (1)$$

where T_b is the brightness temperature, which in the Rayleigh-Jeans approximation is given by:

$$T_b(\nu) = 1.1 \times 10^{-15} \frac{S_\nu}{\nu_{\text{GHz}}^2 \Omega} \text{ [K]}, \quad (2)$$

where S_ν is the integrated flux density in Jy, ν is the frequency in GHz and Ω is the source solid angle in sr. Considering a spherically symmetric, optically thin, homogeneous, ionization-bounded H II region, the emission measure, EM , can be derived from τ_ν using:

$$EM = 12.143 \frac{\tau_\nu}{a_\nu T_e^{-1.35} \nu_{\text{GHz}}^{-2.1}} \text{ [pc cm}^{-6} \text{]}, \quad (3)$$

where a_ν is a correction factor near unity whose exact value depends on the frequency ν and T_e (Mezger & Henderson 1967).

Following the formalism explained by Wood & Churchwell (1989), the rms electron density can be derived from:

$$n_e = 1.4 \times 10^3 \sqrt{\left(\frac{EM}{10^6 \text{ pc cm}^{-6}} \right) \left(\frac{0.5 \text{ pc}}{D} \right)} \text{ [cm}^{-3} \text{]}, \quad (4)$$

where D is the source diameter in pc. Finally, the number of hydrogen ionizing photons ($h\nu > 13.6 \text{ eV}$) per second required to maintain the ionization of the nebula is:

$$N_{\text{Lyc}} = 4.634 \times 10^{46} \left(\frac{T_e}{10^4 \text{ K}} \right)^{-0.45} \left(\frac{\nu_{\text{GHz}}}{5 \text{ GHz}} \right)^{0.1} \left(\frac{R}{1 \text{ kpc}} \right)^2 \times \left(\frac{S_\nu}{1 \text{ Jy}} \right) a_\nu^{-1} \text{ [s}^{-1} \text{]}, \quad (5)$$

where R is the heliocentric distance to the source. This expression assumes that the nebula is dust-free.

The derived physical parameters (diameter, opacity, emission measure, electron density and photon flux of the Lyman continuum) are shown in Table 4. They have been computed for $T_e = 7500 \text{ K}$.

Ultracompact H II (UCH II) regions are characterized by their small sizes (diameter $\leq 0.05 \text{ pc}$) and high densities ($n_e \geq 10^4 \text{ cm}^{-3}$), while classical H II regions have diameters $\geq 0.5 \text{ pc}$ and densities $\leq 10^3 \text{ cm}^{-3}$ (Garay & Lizano 1999). The characteristics of compact H II (CH II) regions are in between those of the ultracompact and classic ones. Among the total of 19 individual objects observed by the ATCA, only IRAS 17160 E can be classified as an UCH II region; from the rest, approximately 13 can be defined as CH II regions and 5 (IRAS 11143, IRAS 12063, IRAS 12331, IRAS 17160 A and IRAS 17221) as classical H II regions.

Wood & Churchwell (1989) identified five morphological classes of UCH II and CH II regions based on the appearance of their radio continuum emission distributions with a spatial resolution of $0.4''$: cometary, core-halo, shell, irregular or multiple peaked and spherical or unresolved. From the ATCA sample, we can identify 3 cometary sources (IRAS 10589, IRAS 15384 and IRAS 17160 C) and 2 core-halo sources (IRAS 12073 A and IRAS 15502 A). Six are spherical or unresolved (IRAS 15502 B, IRAS 17160 B-D-E and IRAS 17279 C-B). The rest are complex sources with multiple embedded components.

4.1. The n_e – D relation

The left panel in Fig. 5 shows a plot of the electron density against the diameter for all the sources listed in Table 4. The objects observed by the ATCA are plotted as filled circles, and those observed by the VLA as open circles. There is a clear

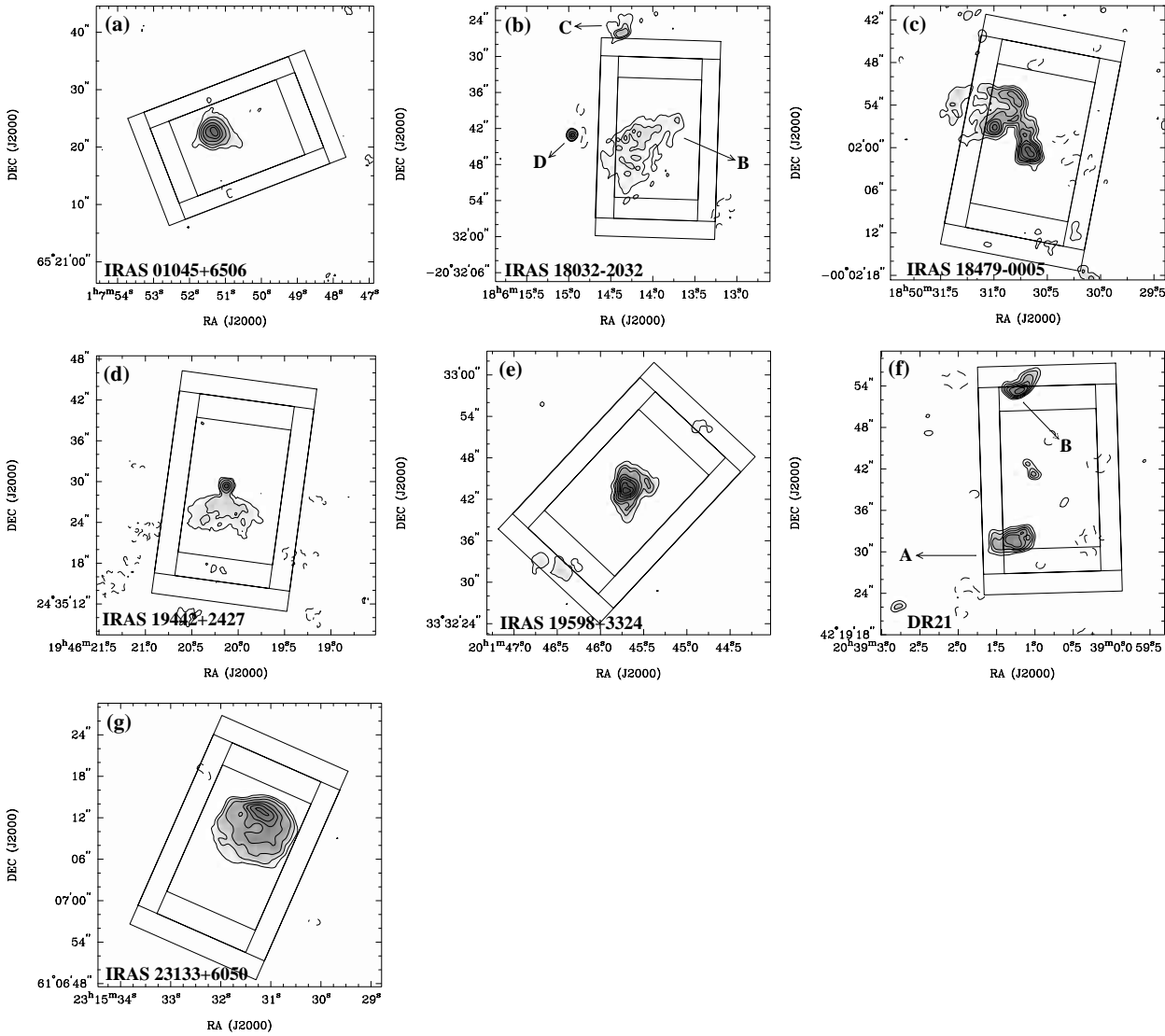


Fig. 4. VLA radio continuum maps. The 4 ISO SWS beams are plotted. Contour levels are: **a)** $-3, 3, 9, 20, 40, 60$ and 75 times the image rms $\sigma = 0.29$ mJy beam $^{-1}$; **b)** $-3, 3, 4, 5, 15$ and 30 times the image rms $\sigma = 1.24$ mJy beam $^{-1}$; **c)** $-3, 3, 9, 20, 30, 50, 80$ and 140 times the image rms $\sigma = 1.30$ mJy beam $^{-1}$; **d)** $-3, 3, 5, 15, 40$ and 70 times the image rms $\sigma = 0.19$ mJy beam $^{-1}$; **e)** $-3, 3, 9, 15, 30, 50, 70, 90$ and 110 times the image rms $\sigma = 2.57$ mJy beam $^{-1}$; **f)** $-3, 3, 6, 10, 15, 20$ and 30 times the image rms $\sigma = 2.75$ mJy beam $^{-1}$. **g)** $-3, 3, 5, 9, 15, 20, 25$ and 30 times the image rms $\sigma = 0.74$ mJy beam $^{-1}$.

correlation between these two physical parameters. A least squares fit to the trend gives a slope of -0.93 ± 0.10 and an intercept of 3.04 ± 0.08 . These fit parameters are in excellent agreement with those derived by Garay et al. (1993) for a large sample of H II regions observed by the VLA. The dotted curves in the figure corresponds to lines of constant number of ionizing photons (10^{47} , $10^{48.5}$ and 10^{50} photons s^{-1}) when the ionized nebula is described by a Strömgen sphere. The trend slope observed by the data is clearly shallower. Following the discussion by Garay & Lizano (1999), we also plot the rate of Lyman ionizing photons (N_{Lyc}) against the diameter, shown in Fig. 5 (right panel). The dotted lines correspond to the cases of Strömgen spheres with $n_e = 10^{2.5}$ and $10^{4.5}$ cm^{-3} . At first sight, and as it has been stated by Garay et al. (1993) and Garay & Lizano (1999), both figures seem to indicate that, on

average, ultracompact H II regions are ionized by stars with lower number of ionizing photons (i.e. by later type stars) than those ionizing compact and classic H II regions. This is not the only possible explanation. Several other effects can cause the n_e - D relation to be shallower than predicted for a pure hydrogen Strömgen sphere. These are:

UCH II regions as density enhancements in larger H II regions – Garay et al. (1993) and Garay & Lizano (1999) suggested that the observed ultracompact H II regions could be density enhancements in more extended H II regions. The contribution of the extended component could be missing from the interferometric observations. If this were the case, then the value of N_{Lyc} would be underestimated for these sources. This effect would make the n_e - D relation shallower.

Table 4. Derived parameters from the ATCA and VLA radio continuum observations. Given are the Galactocentric and heliocentric distance, the observed frequency used in the calculations and the derived parameters: linear diameter, opacity, emission measure, electron density and number of ionizing photons required to maintain the ionization of the nebula. The IRAS luminosity is given in the last column.

Source	R_{Gal} (kpc)	R (kpc)	Radio properties							
			ν (GHz)	Diameter [†] (pc)	τ_{ν}	EM (10^6 pc cm^{-6})	n_e (10^3 cm^{-3})	$\log N_{\text{Ly}\alpha}$ (s^{-1})	L/L_{\odot} (10^4)	
IRAS 01045	13.8	7.0	8.4	0.16	0.03	5.2	5.7	47.82	4.10	
IRAS 10589	9.5	8.0	4.8	0.50	0.06	3.2	2.5	48.62	29.4	
IRAS 11143	9.7	8.8	4.8	2.82	0.005	0.3	0.3	49.05	17.1	
IRAS 12063	9.3	9.5	4.8	1.22	0.02	1.2	1.0	48.97	45.0	
IRAS 12073	A	10.1	10.8	4.8	0.41	0.6	35.5	9.3	49.49 ^Δ	400
...	B	0.37	0.2	10.1	5.2	48.85	...	
IRAS 12331	6.9	4.5	4.8	1.47	0.006	0.3	0.5	48.58	8.45	
IRAS 15384	6.4	2.7	4.8	0.53	0.02	1.3	1.6	48.26	10.1	
IRAS 15502	A	4.5	7.0	4.8	0.16	0.7	37.5	15.3	48.68 [*]	131
...	B	0.08	0.3	16.7	14.0	47.78	...	
IRAS 16128	5.5	3.7/11.4	8.6	0.32/0.98	0.05	8.8	5.2/3.0	48.65/49.63 [◻]	22.8/216	
IRAS 17160	A	3.0	5.7/11.0	8.6	0.62/1.20	0.01	2.2	1.9/1.3	48.63/49.21 [◻]	35.6/133
...	B	...	h	...	0.09/0.17	0.02	3.1	5.9/4.3	47.09/47.66	...
...	C	...	h	...	0.07/0.14	0.02	3.5	6.9/4.9	47.00/47.56	...
...	D	...	h	...	0.06/0.12	0.1	21.8	18.9/13.6	47.61/48.18	...
...	E	...	h	...	0.03/0.06	0.08	15.3	22.4/16.1	46.85/47.42	...
IRAS 17221	5.2	3.4/13.4	4.8	1.10/4.35	0.005	0.3	0.5/0.3	48.25/49.44	7.52/117	
IRAS 17279	A	3.4	5.1/11.8	8.6	0.49/1.14	0.003	0.6	1.1/0.7	47.88/48.61 [Ⓜ]	10.4/55.9
...	B	...	h	4.8	0.07/0.15	0.1	6.3	9.7/6.4	47.15/47.88	...
...	C	...	h	...	0.08/0.19	0.09	4.8	7.6/5.0	47.23/47.96	...
IRAS 18032	B	3.0	5.7	8.4	0.38	0.006	1.1	1.7	47.92 [Ⓢ]	32.3
...	C	0.11	0.01	2.1	4.3	47.11	...
...	D	0.03	0.2	31.2	33.6	47.08	...
IRAS 18479	A	7.4	13.0	8.4	0.30	0.1	27.0	9.4	49.10 [◊]	147
...	B	0.09	0.6	119.9	35.5	48.74	...
IRAS 19442	core	7.7	2.0	8.4	0.01	0.08	14.6	34.8	46.45 [♯]	3.39
...	halo	0.11	0.002	0.3	1.6
IRAS 19598	9.6	8.2	8.4	0.25	0.3	44.3	13.4	49.14	187	
DR21	A	8.6	2.8	8.4	0.05	0.1	20.5	20.4	47.39	^c
...	B	0.06	0.1	21.1	18.8	47.58	...
IRAS 23133	12.6	6.7	8.4	0.2	0.02	4.3	4.2	48.10	27.5	

[†] Diameter in pc of the sphere assumed to be representative of the source (see Sect. 4). ^Δ $10^{49.95}$ photons s^{-1} are required to ionize the whole nebula, including the contribution of the low brightness emission. ^{*} $10^{48.73}$ photons s^{-1} are required to ionize both components A and B. [◻] $10^{48.83}/10^{49.80}$ photons s^{-1} result when the total 4.8 GHz flux density is considered. [◻] $10^{48.97}/10^{49.54}$ result when the total 4.8 GHz flux density integrated over the whole field is considered. [Ⓜ] $10^{48.32}/10^{49.05}$ photons s^{-1} result when the total 4.8 GHz flux density integrated over the whole field is considered. [Ⓢ] The added contribution of the 3 components A, B and C is $10^{48.03}$ photons s^{-1} . ^h We consider it to be located at the same distance than the IRAS source. [◊] $10^{49.40}$ photons s^{-1} are required to ionize the whole nebula. [♯] Lyman continuum flux required to maintain the ionization of the whole nebula. ^b The added contribution of the 2 components A and B is $10^{47.80}$ photons s^{-1} . ^c No IRAS fluxes available.

Optical depth effects – the radio emission of UCH II regions, and perhaps also CH II regions, might be affected by optical depth effects. Correcting for this would shift the points upward in Fig. 5 (left panel), thus making the relation steeper. Although the opacities listed in Table 4 seem to indicate that all the H II regions are optically thin even at 4.8 GHz, this effect cannot be ruled out completely, as, in some cases, UCH II regions are well known to be optically thick at this frequency.

Clumpiness – H II regions are found to be rather clumpy, with typical filling factors of the order of ~ 0.1 (e.g. Copetti et al. 2000). For an H II region with a given $N_{\text{Ly}\alpha}$, a decrease of the filling factor will result in an increase of the region size. It seems reasonable to consider that clumpy H II regions are more easily found among large H II regions rather than among more compact, small ones. Hence, in this case, the diameter measured in clumpy, large H II regions should be larger

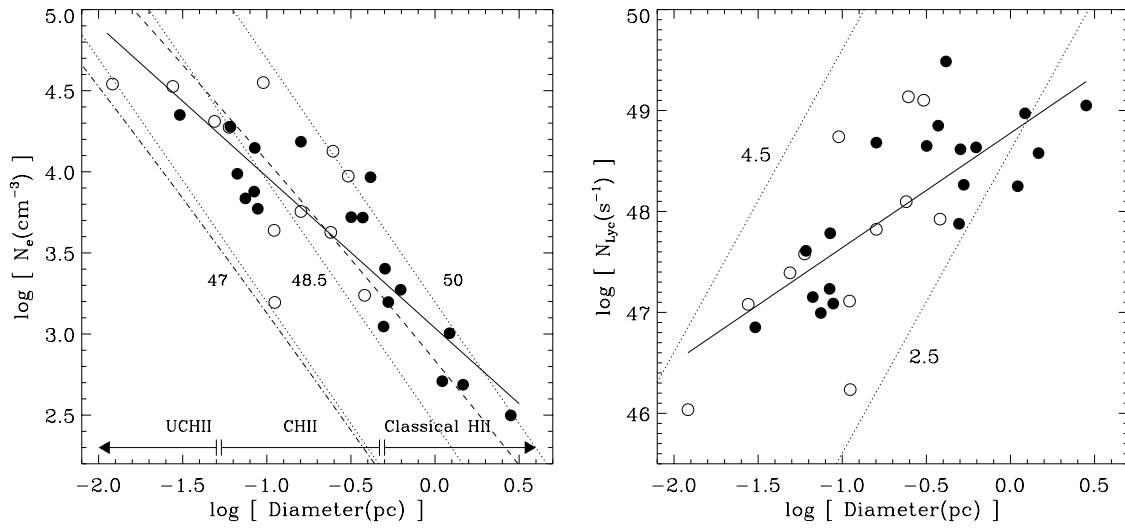


Fig. 5. *Left:* plot of the rms electron density against the linear source diameter. The ATCA sample is represented by filled circles and the VLA sample by open circles. The solid line is a least-squares fit to the data. The dotted curves are lines of constant number of ionizing photons (10^{47} , $10^{48.5}$ and 10^{50} photons s^{-1}) for pure Strömgren spheres. The dotted-dashed and dashed lines show the effect of dust on the size of an H II region with $N_{\text{Ly}\alpha} = 10^{47}$ and 10^{50} photons s^{-1} , respectively, and a standard dust-to-gas ratio of 1. The typical classification of ultracompact (UCH II), compact (CH II) and classic H II regions is given at the bottom of the plot according to their linear sizes. *Right:* plot of the rate of Lyman ionizing photons against the linear source diameter. The solid line is a least-squares fit to the data. The dotted lines represent the $N_{\text{Ly}\alpha} - D$ relations for a Strömgren sphere without dust and density $n_e = 10^{2.5}$ and $10^{4.5}$ cm^{-3} .

than the one predicted by the Strömgren theory, shallowing the $n_e - D$ relation (see right panel in Fig. 5).

Presence of dust within the ionized gas – if a significant fraction of the stellar UV radiation is absorbed by dust within the ionized gas, the free-free flux will be then reduced and consequently, $N_{\text{Ly}\alpha}$ will be just a lower limit of the true stellar ionizing flux. We can apply here the simple analysis for dusty Strömgren spheres by Petrosian et al. (1972), which present approximate analytical expressions to describe the effect of internal dust on the ionization structure of H II regions. The size of an H II region with dust uniformly distributed throughout the ionized gas can be found by setting the left-hand side of Eq. (6) in Petrosian et al. (1972) equal to zero. The effect of dust on the size of an H II region with $N_{\text{Ly}\alpha} = 10^{47}$ and 10^{50} photons s^{-1} , and a standard dust-to-gas, corresponding to an EUV absorption cross section of 10^{-21} cm^2 (H-atom) $^{-1}$, is indicated in Fig. 5 (left panel). The effect of dust is to flatten the relation found in the case of a pure, dust-free Strömgren sphere. The larger the dust absorption cross section per H atom, the shallower the relation between n_e and D . This is because the absorption optical depth of dust is proportional to $n_e^{1/3}$. Consequently, for a particular dust-to-gas ratio, higher densities lead to higher dust optical depths, and thus, to a higher number of ionizing photons absorbed by the dust; as a result, a larger fraction of the EUV photons produced by the star go directly into heating the dust rather than ionizing the gas, and the resulting H II region is smaller.

Within this interpretation, the shallow slope of the $n_e - D$ relation is due to the effect of dust. Since only a few points are expected to have $N_{\text{Ly}\alpha} > 10^{50}$ photons s^{-1} , the case of a

dusty H II region with $N_{\text{Ly}\alpha} = 10^{50}$ photons s^{-1} represents almost an upper limit to n_e for a given D . The dust abundance must be highly variable then, since there are some high density nebulae (clustered around $n_e = 10^4$ cm^{-3} and $D = 10^{-0.5}$ pc) close to the dust-free Strömgren sphere solution for $N_{\text{Ly}\alpha} = 10^{50}$ photons s^{-1} . This is close to the upper limit for O stars and hence they must represent regions with little dust.

The abundance of dust in H II regions has been a topic of much controversy. Earlier estimates (Natta & Panagia 1976; Tielens & de Jong 1979), based upon fitting the spectral energy distribution, lead to controversial results mainly reflecting the lack of spatial resolution at far-IR wavelengths. More recent studies (Chini et al. 1986; Churchwell et al. 1990), based upon studies of specific compact H II regions, suggest somewhat depleted dust abundances in the ionized gas. But the inherent uncertainty in the stellar parameters preclude strong conclusions. Theoretically, dust could be sputtered in the hot ionized gas (e.g. Draine & Salpeter 1979) as well as blown out by radiation pressure, and the dust abundance might well be time dependent.

Clusters of ionizing stars – the existence of the trends in Fig. 5 may also represent the effect of stellar clusters on the ionization structure of H II regions. Indeed, the points with $N_{\text{Ly}\alpha} > 10^{48}$ s^{-1} are uniformly distributed between the lines representing pure Strömgren spheres at $n_e = 10^{2.5}$ and $10^{4.5}$ cm^{-3} , whereas at lower $N_{\text{Ly}\alpha}$, the points cluster around the Strömgren sphere solutions for higher densities (cf. right panel in Fig. 5). So, extended, low density H II regions seem to be exclusively powered by early O stars (more likely by clusters of OB stars), while the high density and hence compact H II regions can be powered by the whole range of O and late B stars. As a

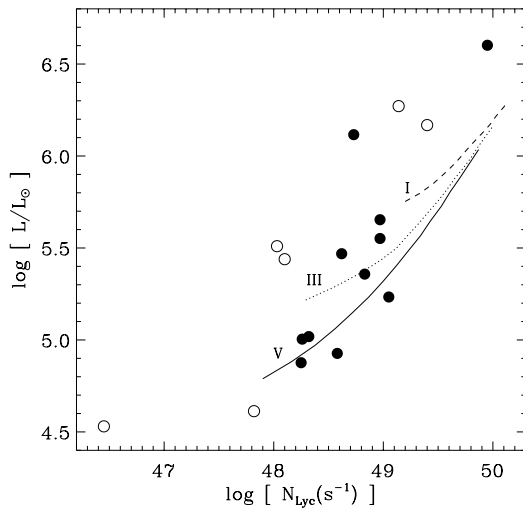


Fig. 6. Plot of the total stellar luminosity against the rate of Lyman ionizing photons. The ATCA sample is represented by filled circles and the VLA sample by open circles. The lines represent the behaviour of a single embedded main sequence (solid), class III (dotted) and class I (dashed) late B/O star. These lines are based on the calibration of early type stars made by Vacca et al. (1996).

corollary, this would imply that the explanation given by Garay & Lizano (1999), i.e. that UCH II regions are excited by later type stars than extended H II regions, is wrong.

There are thus many factors that may influence the relationship between the density and diameter of H II regions (or equivalently, the relationship between $N_{\text{Ly}\alpha}$ and the diameter). However, it is difficult to discriminate among these possible factors on the basis of the present data.

4.2. Stellar content

Finally, we can consider general properties of the stars ionizing the H II regions. The infrared luminosity is produced by thermal emission from dust heated by all wavelengths of stellar radiation and thus, it is an approximation to the total luminosity, L , of the star or stars embedded in the nebula. We take the IRAS infrared luminosities derived in Peeters et al. (2002b). Because of the large IRAS beam, the $N_{\text{Ly}\alpha}$ value suitable to compare with the IRAS luminosity is that which accounts for the ionization of the whole nebula and therefore, we need to sum the contribution of the various components in the case of complex sources.

The comparison of the stellar luminosity and Lyman continuum photon flux is shown in Fig. 6. The curves represent the behaviour of a single embedded main sequence, class III and class I late-B/O star based on the calibration by Vacca et al. (1996). In general, the observed values of $N_{\text{Ly}\alpha}$ and L are in the range of those predicted to be typical of early B and O stars. However, a large fraction of the sources lie above the theoretical predictions for single stars, indicating that a single star cannot account by itself for all the integrated stellar luminosity. Radio morphologies of many of the sources show indeed multiple components. We note, however, that the IRAS beam

is large ($\sim 1.5'$) and may include more sources than the radio components observed. Also, the derived $N_{\text{Ly}\alpha}$ values must be taken as a lower limit if part of the radio flux is missing from our interferometric observations. The combined effect of these two facts would shift points in Fig. 6 down and to the right, thus improving the correlation.

5. Combining ISO and radio observations

The comparison of the radio continuum observations with the ISO spectroscopic data allows us to further characterize the physical properties of the H II regions. In particular, it allows us to study the extinction in the infrared towards the nebulae, determine elemental abundances of elements such as nitrogen, neon, sulphur and argon, and constrain the properties of the ionizing stars. This comparison, however, requires a detailed analysis of the radio continuum images in order to determine the total radio flux density associated with the region observed by every Short Wavelength (2.3–45 μm , SWS) and Long Wavelength (43–196 μm , LWS) Spectrometer aperture (see Peeters et al. 2002b for a full description of the ISO instrument).

The characterization of the SWS beam profiles is described in Salama (2000). Basically, each SWS beam profile results from the convolution of the telescope point spread function with the entrance slit, and then with the detector response profile. A different beam profile exists, therefore, for every detector (12 in total). Because of imaging defects inside the instrument, these beam profiles were found to significantly deviate from the predicted shapes. Large differences between the beam profiles are seen along the cross-dispersion direction (cf. Fig. 7): the shapes of the band 1 and band 2 profiles are triangular; the band 3 profiles, although closer to top-hat profiles, are off-center; the band 4 profile resembles a broad, off-center Gaussian. The shapes of the beam profiles have been modeled and included as standalone calibration files (*cal36*) in the pipeline version 10. Using these files, an appropriate mask has been created for every source and detector at the correct orientation and center position. Afterwards, the original radio maps have been multiplied by these masks and an integrated flux density derived. In the case of the ATCA data, we use the 4.8 GHz maps because of their higher sensitivity to large scale structure. The integrated flux densities which resulted from this analysis are presented in Table 5. The variations in these resulting flux densities depend on the source morphology and orientation of the SWS beams. The bottom right panel in Fig. 7 shows how the flux densities for two extreme cases (IRAS 10589 and IRAS 16128) vary with the SWS band. While the integrated flux densities derived for IRAS 10589 are practically constant, in the case of IRAS 16128, the radio flux integrated over the SWS band 4 aperture is 5 times larger than the one integrated over the SWS band 1A. This happens because IRAS 16128 is much larger than the SWS beams and it is not centered within the apertures.

The LWS beam profile has been recently described by Lloyd (2001). The size of the aperture, initially assumed to be circular with a diameter of $100''$, has been found to be significantly smaller for reasons which are not entirely known.

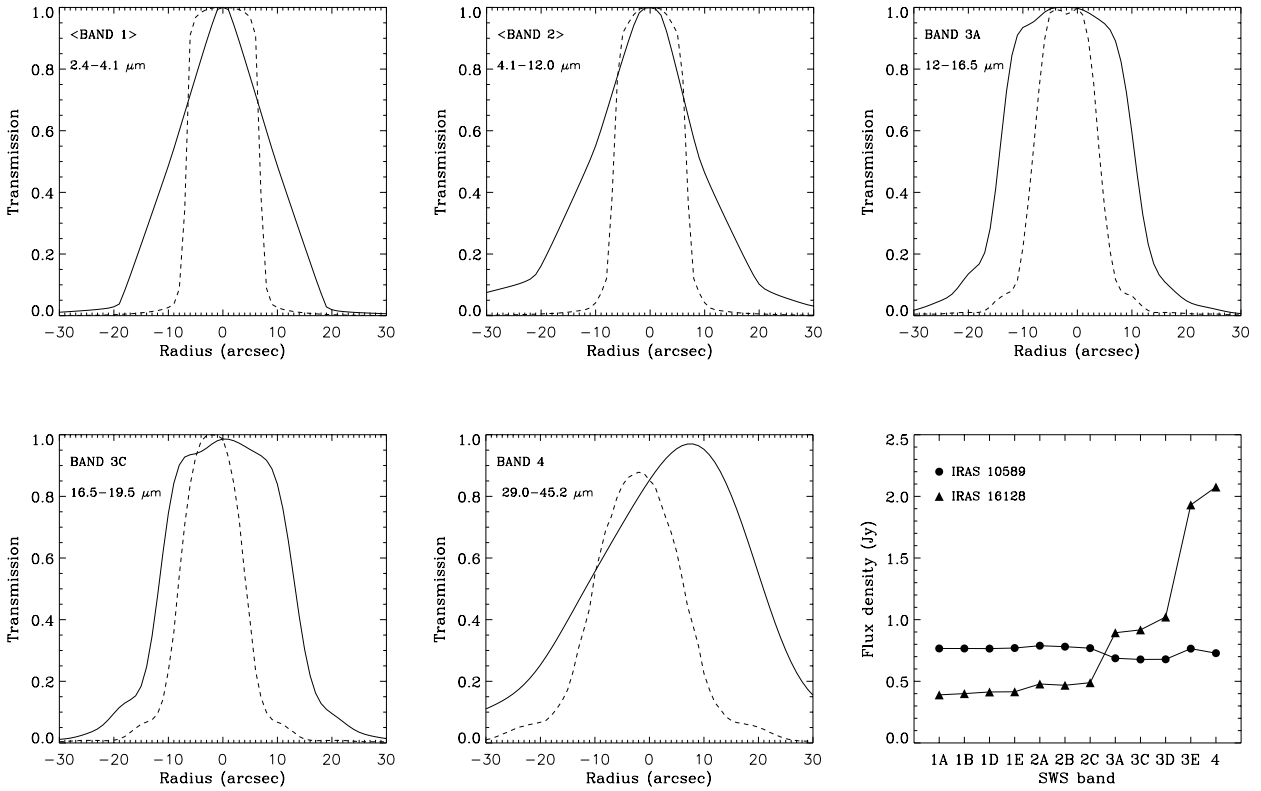


Fig. 7. SWS beam profile models along the cross-dispersion direction (solid line) and dispersion direction (dashed line). *Top left:* average beam profile of SWS bands 1A, 1B, 1D and 1E. *Top middle:* average beam profile of SWS bands 2A, 2B and 2C. *Top left:* beam profile of band 3A. *Bottom right:* beam profile of band 3C. *Bottom middle:* beam profile of band 4. *Bottom right:* variations of the 4.8 GHz flux density integrated over the 12 SWS beams for IRAS 10589 and IRAS 16128.

The best value for most of the detectors is close to $80''$; somewhat smaller for the long wavelength detectors. Furthermore, the beam profile is also slightly asymmetric because of instrumental effects. The observed profiles for the short wavelength detectors are close to a top-hat profile, while they become more Gaussian towards longer wavelengths. We computed two different masks: one being a Gaussian with a $80''$ FWHM, and the other a top-hat profile with a circular base of $80''$. Two different integrated radio flux densities result from using either one or the other mask. The last column in Table 5 quotes the averaged value of these two integrated flux densities, the number in brackets being the difference between the two methods. This difference is less than 10% for all the sources.

5.1. Extinction in the near-infrared

H II regions can be embedded in dust and molecular gas and suffer from extinction of their radiation by dust located either within the ionized gas or in the neutral foreground material. In the Galaxy, the pathlengths to H II regions in the disk are often long causing a large extinction. The extinction in the visible for compact H II regions ranges from a few tens to hundreds of magnitudes.

The radio continuum measurements do not suffer from extinction and allow us to determine directly the intrinsic flux,

$F_o(\lambda)$, of any H I recombination line. The flux of an infrared H I line with wavelength λ observed by ISO, $F(\lambda)$, can then be expressed as:

$$F(\lambda) = F_o(\lambda)10^{-0.4A_\lambda}, \quad (6)$$

where $F_o(\lambda)$ is the intrinsic line flux derived from the radio flux and A_λ is the extinction at the wavelength λ of the infrared line. $F_o(\lambda)$ can be determined from radio observations using:

$$F_o(\lambda) = \epsilon_\lambda EM \left(\frac{n_p}{n_e} \right) \frac{\Omega}{4\pi}, \quad (7)$$

where ϵ_λ is the emissivity coefficient of the H I line with wavelength λ (Hummer & Storey 1987). Considering a spherically symmetric, optically thin, homogeneous, ionization-bounded H II region, the above expression for $F_o(\lambda)$ can be written as:

$$F_o(\lambda) = 9.70 \times 10^{13} \epsilon_\lambda T_e^{0.35} \nu_{\text{GHz}}^{0.1} S_\nu \left(\frac{n_p}{n_e} \right) [\text{ergs}^{-1} \text{cm}^{-2}], \quad (8)$$

where ϵ_λ is expressed in $\text{erg s}^{-1} \text{cm}^3$, T_e in K, ν in GHz and S_ν is the radio continuum flux density in Jy measured at frequency ν . The H I line emissivities are proportional to $T_e^{-\alpha}$. For instance, from a fit to the Brackett α ($4.05 \mu\text{m}$, Br α) line emissivities computed by Storey & Hummer (1995), we find that $\alpha \sim -1.23$. In this case, $F_o(\lambda)$ in Eq. (8) varies with electron temperature as $T_e^{-0.88}$. In the following, we will consider

Table 5. Radio flux densities integrated over the 12 SWS apertures and the LWS aperture. The official band range in μm is given for every aperture.

Source	Integrated flux density (mJy)												
	1A (2.38–2.61)	1B (2.60–3.03)	1D (3.02–3.53)	1E (3.52–4.06)	2A (4.05–5.31)	2B (5.30–7.01)	2C (7.00–12.1)	3A (12.0–16.6)	3C (16.5–19.6)	3D (19.5–27.6)	3E (27.5–29.0)	4 (28.9–45.2)	LWS* (43.0–196.0)
IRAS 01045	205	204	205	206	210	210	207	230	235	232	238	230	†
IRAS 10589	766	766	765	770	789	781	769	687	677	678	765	728	1210 (19)
IRAS 11143	284	284	286	288	318	315	314	332	333	345	479	554	1981 (79)
IRAS 12063	1261	1261	1272	1267	1300	1278	1269	1484	1437	1441	1534	1481	1959 (23)
IRAS 12073	3655	3660	3684	3702	3936	3886	3864	4906	4708	4919	4765	5502	14092 (889)
IRAS 12331	231	233	236	238	278	274	277	338	342	371	584	707	3059 (310)
IRAS 15384	1495	1496	1506	1508	1581	1559	1549	1756	1719	1749	1956	2064	4435 (208)
IRAS 15502	1342	1341	1367	1344	1362	1286	1269	1668	1642	1597	1952	1875	2707 (85)
IRAS 16128	390	400	413	415	478	468	489	894	917	1021	1931	2076	7468 (428)
IRAS 17160	563	567	578	575	621	605	611	860	850	890	1223	1300	3940 (267)
IRAS 17221	343	344	347	349	392	386	385	405	419	431	636	731	2451 (181)
IRAS 17279	187	187	187	189	198	196	194	183	185	193	253	282	930 (23)
IRAS 18032	367	367	366	369	380	375	367	288	285	292	349	340	609 (11)
IRAS 18479	2137	2136	2128	2138	2151	2120	2087	1740	1710	1712	2044	1880	2751 (29)
IRAS 19442	73	73	73	73	76	75	75	69	65	65	64	61	93 (2)
IRAS 19598	3348	3348	3351	3353	3401	3410	3396	3352	3326	3264	3348	3030	3662 (29)
DR21	604	603	601	608	640	623	609	381	443	444	694	786	1556 (52)
IRAS 23133	619	619	621	622	626	621	613	670	672	654	702	669	738 (3)

† No LWS observation available. * Given is the average of the integrated flux density obtained from two different methods (see Sect. 5). The number in brackets is the difference in mJy between these two methods.

Table 6. Extinction in K (2.2 μm) calculated by (1) using Eq. (9), and (2) using the Br β /Br α decrement observed by ISO (unless otherwise is indicated).

Source	A_K (1) [‡]	A_K (2)	Source	A_K (1) [‡]	A_K (2)
IRAS 01045	3.2 \pm 1.4	(1) ‡	IRAS 17160	5.6 \pm 0.3	(1) 5.8 \pm 2.3*
IRAS 10589	1.3 \pm 0.1	(4) 1.5 \pm 0.5	IRAS 17221	1.8 \pm 0.2	(2) 1.8 \pm 0.4
IRAS 11143	0.8 \pm 0.1	(2) <0.6	IRAS 17279	2.2 \pm 0.5	(1) ‡
IRAS 12063	1.5 \pm 0.1	(6) 0.8 \pm 0.5	IRAS 18032	1.1 \pm 0.3	(1) ‡
IRAS 12073	1.47 \pm 0.06	(9) 0.8 \pm 0.2	IRAS 18479	7.8 \pm 0.2	(1) ‡
IRAS 12331	1.3 \pm 0.3	(1) ‡	IRAS 19442	<1.8	‡
IRAS 15384	1.53 \pm 0.09	(6) 1.3 \pm 0.3	IRAS 19598	2.49 \pm 0.05	(9) 1.6 \pm 0.2
IRAS 15502	3.1 \pm 0.2	(3) 2.7 \pm 0.6	DR21	2.6 \pm 0.3	(1) 3.1 \pm 0.7*
IRAS 16128	◇	(2) ▷	IRAS 23133	0.4 \pm 0.1	(2) ~0

[‡] Given in brackets is the number of H I lines used in the calculation (see text). [‡] Only Br α is available from the SWS spectrum. ◇ Two lines (Br α and Br β) are observed by the ISO-SWS, but the A_K extinctions derived from them are very different (2.3 \pm 0.3 and 0.8 \pm 0.2, respectively).

[▷] The Br α /Br β decrement is not consistent with a $\lambda^{-\alpha}$ law. * Calculated using the Pf α /Br α decrement.

a ratio of protons to electrons $n_p/n_e \approx 0.90$ and $T_e = 7500$ K, typical for Galactic H II regions (Shaver et al. 1983; Afflerbach et al. 1996, 1997; Deharveng et al. 2000). According to the above T_e dependence, a variation in T_e of 3000 K would only change $A_{\text{Br}\alpha}$ by ~ 0.3 mag.

At infrared wavelengths between 1 and 7 μm , the extinction law, as based on *JHK* photometry, appears to be independent of the line-of-sight and consistent with a simple power law $A_\lambda = A_K(\lambda/2.2)^{-1.7}$ (Mathis 1990; Martin & Whittet 1990), with A_K the extinction in the K-band (2.2 μm). Assuming this extinction law, we can determine a value for A_K from any of the H I recombination lines observed by ISO. Combining the above equations, the expression for A_K is:

$$A_K = 2.5 \left(\frac{\lambda}{2.2} \right)^{1.7} \log \left(\frac{F_o(\lambda)}{F(\lambda)} \right). \quad (9)$$

Most of the sources have more than one observed H I line from which an “independent” measurement of A_K can be obtained. The H I lines up to 7 μm have been observed by either the SWS band 1 or 2. The 4.8 GHz flux densities integrated over these detector apertures are quoted in Table 5. We use these flux densities to predict the non-extincted H I line flux (Eq. (8)). For every observed H I line we derive a value for A_K (Eq. (9)) with a 1σ uncertainty propagated from the error in the ISO H I line flux and the radio flux density. Finally, we compute the weighted mean to get the final result. Table 6 shows the final value for A_K and, in brackets, the number of H I lines present in the ISO SWS spectrum that have been used to compute the mean. Table 6 contrasts the A_K obtained via this method to those obtained by comparing the observed Br β /Br α (or Pf α /Br α) decrement with the Case B approximation (Osterbrock 1989) and reported in Martín-Hernández et al. (2002a).

5.2. Extinction in the mid-infrared

The extinction in the 8–20 μm regime is dominated by the 9.7 and 18 μm absorption features, attributed to the Si-O stretch

and Si-O-Si bending modes in silicates. The strength and profile of these bands have been extensively studied (see, e.g., the review by Draine 1989). The “astronomical silicate” by Draine & Lee (1984) and Draine (1985) is widely used to describe the profiles of these 9.7 and 18 μm absorption features. The “astronomical silicate” was constructed to be consistent with the available observations, and it is based on the “Trapezium” emissivity profile for $\lambda < 13$ μm and observations of both extinction and emission at longer wavelengths. This normalized profile is shown in Fig. 8. A λ^{-2} law is assumed for $\lambda > 20$ μm . The positions of the main mid-infrared fine-structure lines are indicated: [Ar III] 9.0, [S IV] 10.5, [Ne II] 12.5, [Ne III] 15.5 and [S III] 18.7 μm .

Two ionic species, S III and Ne III, present two emission lines well separated in wavelength. If we assume that the emission of these lines is uniform, the non-extincted ratio of the two lines of any of these ionic species can be simply written as:

$$\left(\frac{X_{\lambda_1}}{X_{\lambda_2}} \right)_o = \frac{\epsilon_{\lambda_1} S_1}{\epsilon_{\lambda_2} S_2}, \quad (10)$$

where the ϵ_λ 's are the emission coefficients and the S 's are the flux densities obtained by integrating over the same aperture where the infrared line emission is measured. As the extinction affecting the line at the longest wavelength is negligible, the comparison between the theoretical line ratio obtained via Eq. (10) and the observed line ratio gives directly the extinction at the shortest wavelength. However, the emissivities of these lines, although independent of the electron temperature, are a strong function of the electron density. In this respect, [S III] 33/19 is very sensitive to electron densities around 10^3 – 10^4 cm^{-3} , which are comparable to the rms densities obtained from the radio continuum observations (cf. Table 4). Therefore, the use of this ratio is not straightforward. Fortunately, the critical densities of the [Ne III] 15 and [Ne III] 36 μm lines are much higher (1.8×10^5 and 2.6×10^4 cm^{-3} , respectively) and one can simply consider the

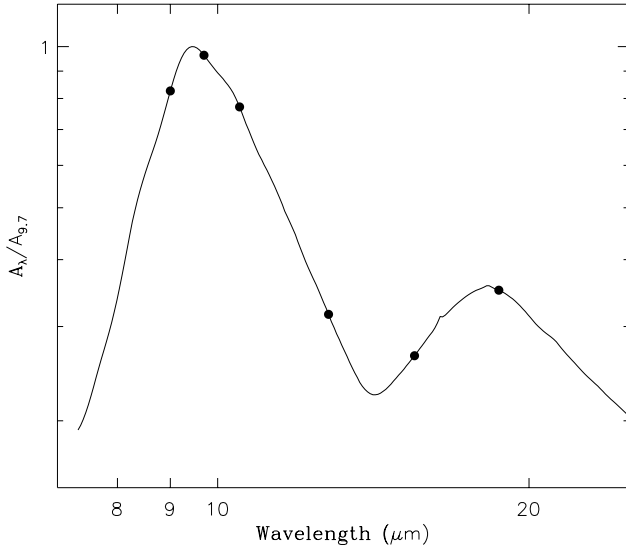


Fig. 8. Normalized “astronomical silicate” profile adapted from the synthetic extinction curve by Weingartner & Draine (2001). The positions of the mid-infrared fine-structure lines are indicated by filled circles.

low density limit to evaluate the line emissivities in Eq. (10). This equation then becomes:

$$\left(\frac{[\text{Ne III}]_{36}}{[\text{Ne III}]_{15}}\right)_o = 0.089 \frac{S_4}{S_{3A}}, \quad (11)$$

where S_{3A} and S_4 are the flux densities integrated over the SWS bands 3A and 4 which measure, respectively, the $[\text{Ne III}] 15$ and $[\text{Ne III}] 36 \mu\text{m}$ lines (cf. Table 5). Comparing with the observed ratio, we can write:

$$\left(\frac{[\text{Ne III}]_{36}}{[\text{Ne III}]_{15}}\right)_o = \left(\frac{[\text{Ne III}]_{36}}{[\text{Ne III}]_{15}}\right)_{\text{obs}} \times 10^{-0.4A'_{15.5}}, \quad (12)$$

and taking $A'_{15.5}$ as the extinction at $15.5 \mu\text{m}$ relative to A_K :

$$\log\left(\frac{[\text{Ne III}]_{36}}{[\text{Ne III}]_{15}}\right)_{\text{obs}} = \log\left(\frac{[\text{Ne III}]_{36}}{[\text{Ne III}]_{15}}\right) + 0.4A'_{15.5}A_K. \quad (13)$$

When plotting the observed line ratio versus the theoretical as in Fig. 9, the intercept gives us $A'_{15.5}$. Assuming that the extinction in the mid-infrared is given by the “astronomical silicate” profile shown in Fig. 8, we find that $A'_{15.5} = 0.275(A_{9.7}/A_K)$, where $A_{9.7}$ is the extinction at the peak wavelength of the $9.7 \mu\text{m}$ silicate feature. The $A_{9.7}/A_K$ value is somewhat controversial and may actually change with position in the Galaxy from about 0.5 locally (Roche & Aitken 1984) to 1.0 towards the Galactic Center (Rieke & Lebofsky 1985; Roche & Aitken 1985). The data seems to agree slightly better with a $A_{9.7}/A_K$ value of 1.0 (cf. Fig. 9) but 0.5 is also acceptable. Therefore, although there may be sources with enhanced silicate strength, we adopt a constant value of 0.5.

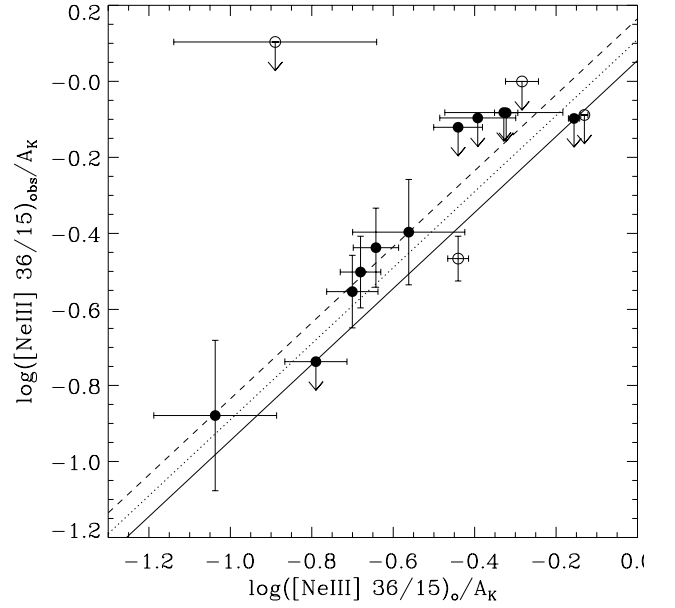


Fig. 9. The observed $[\text{Ne III}]$ line ratio is compared to the theoretical value calculated from the radio continuum emission. Both have been normalized to the A_K extinction calculated in Sect. 5.1. The straight lines correspond to the predictions given for a mid-infrared extinction law with $A_{9.7}/A_K = 0.5$ (solid line), 1.0 (dotted line) and 1.5 (dashed line). The ATCA sample is represented by filled circles and the VLA sample by open circles. IRAS 23133, with an abscissa equal to -2.6 and an upper limit for the ordinate of 1.1 falls out of the plot.

5.3. Elemental abundances

For optically thin infrared lines and radio continuum free-free emission, the abundance of an ion X^{+i} relative to H^+ is given by:

$$\frac{X^{+i}}{\text{H}^+} = 1.03 \times 10^{-14} T_e^{-0.35} \left(\frac{F_o(\lambda, X^{+i})}{\epsilon_\lambda(X^{+i})}\right) \left(\frac{\nu_{\text{GHz}}^{-0.1}}{S_\nu}\right) \frac{n_e}{n_p}, \quad (14)$$

where $F_o(\lambda, X^{+i})$, in units of $\text{erg s}^{-1} \text{cm}^{-2}$, is the extinction-corrected infrared flux of the line produced by the ion X^{+i} with wavelength λ , and $\epsilon_\lambda(X^{+i})$, in units of $\text{erg s}^{-1} \text{cm}^3$, is the corresponding line emission coefficient. This expression assumes that $\epsilon_\lambda(X^{+i})$ is constant over the source. S_ν is the radio continuum flux density at the frequency ν obtained by integrating over the same aperture where the infrared line emission is measured.

Equation (14) shows only a weak dependence on T_e along the typical electron temperatures for H II regions (5000–10 000 K). Likewise, the emission coefficients of fine-structure lines show only a very slight dependence on T_e because these lines are emitted from levels with excitation energies much lower than the mean colliding electron energy. Therefore, we will consider a single T_e of 7500 K. The line emission coefficients, however, depend critically on the nebular electron density, n_e , when n_e is of the order of or larger than the critical density of the upper atomic level (see the detailed discussion in 2002a). At densities much lower than the critical density of the line, the probability of collisional de-excitation is much lower than the radiative transition probability and each collisional excitation produces a photon. The derived abundance is, in this

case, independent of n_e . The line emission coefficients depend also on the atomic parameters (transition probabilities and collisional strengths). We use here the atomic parameters compiled for the analysis in Martín-Hernández et al. (2002a) (cf. Table 1), updating the collisional strengths for the [Ne III] fine-structure lines, for which new values have been calculated by McLaughlin & Bell (2000).

The determination of ionic abundances via Eq. (14) depends critically on: (1) accurate measurement of the radio flux density which matches the infrared line emission observed by ISO; (2) the electron density, n_e , needed to evaluate the line emission coefficients; and (3) the extinction correction applied to the line fluxes.

In the following we discuss how the above factors affect the abundance determination of nitrogen, neon, sulphur and argon.

Nitrogen. The nitrogen lines [N III] 57.3 μm and [N II] 121.7 μm are observed by the large ISO-LWS beam, which has an average diameter of 80". The total 4.8 GHz flux densities integrated over such a beam are reported in Table 5. The critical densities of these lines are quite low: 2.7×10^2 and 1.4×10^3 , respectively for the [N II] and [N III] lines. These critical densities are of the order of the rms electron densities derived for the object sample (cf. Table 4), and therefore, the effect of collisional de-excitation has to be taken into account. The low-density condition cannot hold in this situation. The choice of n_e required to evaluate the line emission coefficients becomes then critical. In Martín-Hernández et al. (2002a) we derived electron densities between $\sim 10^2$ and $\sim 10^3 \text{ cm}^{-3}$ for the sample using the [O III] 52 and 88 μm lines observed by the LWS. Because these [O III] lines have critical densities similar to those of the nitrogen lines and both sets of lines have been observed with roughly the same aperture, the use of these densities seem appropriate. Finally, the extinction of these lines is negligible and the line fluxes listed in Peeters et al. (2002b) can be used directly. The total N/H abundance is calculated by adding the resulting N^+/H^+ and N^{++}/H^+ ionic abundances. The contribution of higher ionization stages to N/H is negligible (see Martín-Hernández et al. 2002a).

Neon. The [Ne II] 12.8 and [Ne III] 15.5 μm lines are observed by the ISO-SWS band 3A. The [Ne III] 36.0 μm line is observed by the larger SWS band 4 aperture. Because of the smaller calibration uncertainties that affect the [Ne III] at the shortest wavelength, we prefer it to the [Ne III] 36.0 μm line to determine the $\text{Ne}^{++}/\text{H}^+$ ionic abundance. The critical densities of the [Ne II] 12.8 and [Ne III] 15.5 μm lines are very high (6.1×10^5 and $1.8 \times 10^5 \text{ cm}^{-3}$, respectively) with respect to the n_e listed in Table 4 and therefore, the low-density limit can be applied in the computation of the emission coefficients. The extinction law considered in Sect. 5.2 gives correction factors $A_{12.8}/A_K = 0.33(A_{9.7}/A_K) = 0.16$ and $A_{15.5}/A_K = 0.27(A_{9.7}/A_K) = 0.14$. The [Ne II] 12.8 and [Ne III] 15.5 μm line fluxes listed in Peeters et al. (2002b) are corrected for extinction using these factors and the A_K obtained in Sect. 5.1. Adding up the resulting Ne^+/H^+ and $\text{Ne}^{++}/\text{H}^+$ ionic abundances, we obtain the total Ne/H abundance. The contribution

of other ionization stages is negligible (see Martín-Hernández et al. 2002a).

Sulphur. The [S III] 18.7, [S III] 33.4 and [S IV] 10.5 μm fine-structure lines are observed by the ISO-SWS bands 3C, 4 and 2C, respectively. Similarly to the case of the [Ne III] lines, the smaller calibration uncertainties of the [S III] 18.7 μm line favours it over the [S III] line at 33.4 μm in the calculation of the S^{++}/H^+ ionic abundance. The critical densities of the [S III] 18.7 and [S IV] 10.5 μm lines (1.0×10^4 and $3.7 \times 10^4 \text{ cm}^{-3}$, respectively), although larger than in the case of the nitrogen lines, are still not much higher than the n_e determined for the objects (cf. Table 4) and thus, collisional de-excitation effects can be important. The density calculated via the LWS [O III] lines may not be representative of the gas where these sulphur lines are formed. Fortunately, the ratio of the two [S III] lines can be used as a diagnostic of the local n_e . In the study presented in Martín-Hernández et al. (2002a) we were unable to use this ratio as a n_e indicator because the lack of spatial information did not allow us to correct the [S III] line ratio for the difference in aperture between the two lines (cf. Fig. 7). The radio continuum observations allow us now to apply such an ‘‘aperture’’ correction. As in Eq. (10), we can write the extinction corrected [S III] line ratio as:

$$\left(\frac{[\text{S III}]_{33.4}}{[\text{S III}]_{18.7}} \right)_o = \frac{\epsilon_{33.4} S_4}{\epsilon_{18.7} S_{3C}}, \quad (15)$$

where S_4/S_{3C} is our ‘‘aperture’’ correction factor. We consider the extinction at 33.4 μm negligible. The extinction at 18.7 μm can be obtained from the extinction derived in Sect. 5.2. We obtain $A_{18.7}/A_K = 0.36(A_{9.7}/A_K) = 0.18$. The resulting electron densities are listed in Table 7. Figure 10 compares these n_e with those derived using the ISO-LWS [O III] line ratio. Both determinations agree very well within the errors, except in the cases of IRAS 18479, IRAS 19598 and IRAS 23133. For these 3 sources, $n_e([\text{S III}])$ is a factor 3–4 higher than $n_e([\text{O III}])$.

The S^{++}/H^+ and S^{+3}/H^+ ionic abundances are calculated using these $n_e([\text{S III}])$ densities. The [S IV] 10.5 μm line used to derive S^{+3}/H^+ is located near the 9.7 μm peak and suffers a high extinction: $A_{10.5}/A_K = 0.80(A_{9.7}/A_K) = 0.40$. The total S/H abundance is calculated by adding up the S^{++}/H^+ and S^{+3}/H^+ ionic abundances. In (Martín-Hernández et al. 2002a) we showed that this approximation underestimates S/H by only a 15%.

Argon. Both the [Ar II] 7.0 and [Ar III] 9.0 μm lines are observed by ISO-SWS band 2C. As in the case of the neon fine-structure lines, the critical densities of these two lines are very high (3.7×10^5 and $2.1 \times 10^5 \text{ cm}^{-3}$, respectively for [Ar II] and [Ar III]) and consequently, the assumption of the low-density limit is valid to evaluate their emission coefficients. Figure 8 shows that the [Ar II] 7.0 μm is located at the minimum of the extinction law. Lutz et al. (1996), using ISO-SWS observations towards Sgr A*, claimed that the extinction curve flattens between 3 and 8 μm and lacks this minimum at 7 μm . However, the study of the extinction between 2 and 7 μm made in Martín-Hernández et al. (2002a) towards a large

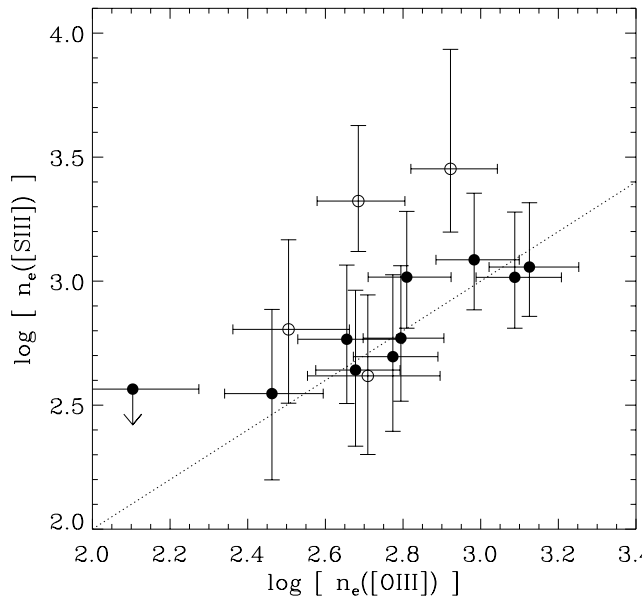


Fig. 10. Comparison between the electron densities calculated by using the LWS [O III] 88/52 μm line ratio and the SWS [S III] 33/19 μm line ratio. The ATCA sample is represented by filled circles and the VLA sample by open circles.

Table 7. Electron densities in cm^{-3} derived using the [S III] 33.4/18.7 μm line ratio.

Source	$([\text{S III}]_{\frac{33.4}{18.7}})_o$	$n_e([\text{S III}])$
IRAS 01045	<0.38	>2582
IRAS 10589	0.71 ± 0.21	1038 (+748, -365)
IRAS 11143	1.29 ± 0.39	352 (+359, -181)
IRAS 12063	0.67 ± 0.20	1140 (+795, -389)
IRAS 12073	0.64 ± 0.20	1219 (+897, -423)
IRAS 12331	0.99 ± 0.30	589 (+486, -243)
IRAS 15384	0.71 ± 0.21	1036 (+739, -363)
IRAS 15502	1.00 ± 0.31	583 (+499, -245)
IRAS 16128	1.55 ± 0.50	217 (+308, -152)
IRAS 17160	1.16 ± 0.36	438 (+417, -207)
IRAS 17221	1.09 ± 0.36	496 (+495, -234)
IRAS 17279	1.99 ± 0.67	<333
IRAS 18032	1.19 ± 0.41	415 (+465, -215)
IRAS 18479	0.36 ± 0.18	2836 (+5764, -1259)
IRAS 19442	1.86 ± 0.73	<467
IRAS 19598	0.44 ± 0.16	2103 (+2137, -786)
DR21	0.95 ± 0.39	639 (+829, -317)
IRAS 23133	0.44 ± 0.16	2140 (+2152, -796)

sample of H II regions (which included IRAS 10589, IRAS 12063, IRAS 12073, IRAS 15384, IRAS 15502 and IRAS 17221) did not show any evidence of this flattening. Considering a power law $A_\lambda \propto \lambda^{-1.7}$, the extinction correction for the [Ar II] line is $A_{7.0}/A_K = 0.14$. The

[Ar III] 9.0 μm line, on the other hand, is located near the 9.7 μm peak and therefore, suffers from large extinction. Assuming the extinction law considered in Sect. 5.2, we obtain $A_{9.0}/A_K = 0.86(A_{9.7}/A_K) = 0.43$. Once the line fluxes are corrected for extinction, we can apply Eq. (14) to derive the Ar^+/H^+ and $\text{Ar}^{2+}/\text{H}^+$ ionic abundances. In Martín-Hernández et al. (2002a) it was showed that the higher ionization stage, $\text{Ar}^{3+}/\text{H}^+$, may contribute to the total Ar/H abundance only at a 30% level for the highest ionized nebula. Therefore, we will neglect its contribution and calculate the total Ar/H by adding up Ar^+/H^+ and $\text{Ar}^{2+}/\text{H}^+$.

The derived elemental abundances of nitrogen, neon, sulphur and argon are listed in Table 8.

Neon, argon and sulphur elemental abundances were calculated in Martín-Hernández et al. (2002a) using $\text{Br}\alpha$ to determine the H^+ emission associated with the nebula. A constant T_e of 7500 K and the low density limit were assumed. These determinations were not corrected for extinction and for the aperture differences between the $\text{Br}\alpha$ and fine-structure lines. Moreover, the assumption of a constant T_e introduced a systematic bias in the sense that a high metallicity nebula, which is expected to have a lower electron temperature, will actually have a higher $\text{Br}\alpha$ emissivity than the one adopted (we note that the $\text{Br}\alpha$ emissivity shows a dependence on the electron temperature that goes as $T_e^{-1.23}$) and vice versa. We find that, on average, the Ne/H abundances determined in Martín-Hernández et al. (2002a) are ~ 1.7 times higher than the ones derived here, while the Ar/H abundances are only ~ 1.2 higher. The sulphur abundances determined in Martín-Hernández et al. (2002a) are, on average, ~ 1.6 times higher, although in some cases, S/H is found to be much lower, which we attribute to the fact that collisional de-excitation effects were not taken into account in the earlier study.

In Sect. 5.2 and in this section, we have used the [Ne III] 36/15 and [S III] 33/19 line ratios to probe the strength of the silicate extinction feature on the one hand, and to determine $n_e([\text{S III}])$ on the other hand. The use of these line ratios, however, yielded inconsistent physical results in the simple analysis presented in Martín-Hernández et al. (2002a). We reproduce here the Fig. 6 used in that paper to illustrate the problem (cf. Fig 11, left panel), where the observed line ratios of [S III] and [Ne III] are compared with their expected values for uniform electron densities between 10^2 and 10^6 cm^{-3} (stars). Meaningful line ratios should lie below their expected values at low densities, i.e., along or to the left of the dashed line in Fig. 11. However, some [S III] line ratios and most of the [Ne III] line ratios are above these limits. This previous study concluded that this discrepancy was largely due to the aperture difference between the lines in these ratios. Most of the objects in our sample show complex and/or extended morphologies, for which the comparison between lines from different apertures is, therefore, not straightforward. However, the radio continuum emission integrated over the SWS apertures can be used as an ‘‘aperture’’ correction. The [S III] and [Ne III] line ratios can consequently be corrected by dividing by the ratio of the radio fluxes in the respective apertures, i.e. S_4/S_{3C} and S_4/S_{3A} , respectively. The right panel in Fig. 11 compares the observed line ratios corrected for the aperture difference with the

Table 8. Ionic and total abundances of N, Ne, S and Ar derived as indicated in Sect. 5.3.

Source	Nitrogen ($\times 10^{-4}$)			Neon ($\times 10^{-4}$)		
	N ⁺ /H	N ⁺⁺ /H	N/H	Ne ⁺ /H	Ne ⁺⁺ /H	Ne/H
IRAS 01045	◇	◇	◇	0.29 ± 0.10	0.08 ± 0.02	0.37 ± 0.12
IRAS 10589	0.50 ± 0.18	0.19 ± 0.06	0.69 ± 0.23	1.16 ± 0.24	0.14 ± 0.03	1.30 ± 0.26
IRAS 11143	0.09 ± 0.04	0.28 ± 0.07	0.37 ± 0.11	0.38 ± 0.08	0.76 ± 0.15	1.14 ± 0.22
IRAS 12063	<0.24	0.26 ± 0.09	<0.59	0.36 ± 0.07	0.31 ± 0.06	0.67 ± 0.13
IRAS 12073	<0.06	0.21 ± 0.07	0.21 ± 0.07	0.17 ± 0.04	0.45 ± 0.09	0.62 ± 0.13
IRAS 12331	0.44 ± 0.16	0.35 ± 0.11	0.79 ± 0.27	1.04 ± 0.21	0.32 ± 0.06	1.36 ± 0.27
IRAS 15384	0.82 ± 0.30	0.39 ± 0.13	1.21 ± 0.43	1.12 ± 0.22	0.15 ± 0.03	1.27 ± 0.26
IRAS 15502	0.63 ± 0.24	0.28 ± 0.08	0.91 ± 0.32	0.54 ± 0.13	0.05 ± 0.01	0.59 ± 0.14
IRAS 16128	0.49 ± 0.18	0.36 ± 0.11	0.85 ± 0.29	0.40 ± 0.07 [†]	0.10 ± 0.02 [†]	0.50 ± 0.08 [†]
IRAS 17160	0.50 ± 0.18	0.15 ± 0.04	0.65 ± 0.22	0.54 ± 0.12	0.04 ± 0.01	0.59 ± 0.13
IRAS 17221	1.18 ± 0.42	0.19 ± 0.06	1.38 ± 0.48	1.52 ± 0.30	0.03 ± 0.01	1.54 ± 0.30
IRAS 17279	1.52 ± 0.50	0.35 ± 0.08	1.87 ± 0.59	2.04 ± 0.43	0.06 ± 0.03	2.09 ± 0.46
IRAS 18032	1.78 ± 0.87	0.31 ± 0.11	2.09 ± 0.99	2.09 ± 0.42	<0.02	2.09 ± 0.42
IRAS 18479	<0.25	0.05 ± 0.02	<0.32	0.45 ± 0.09	0.08 ± 0.02	0.53 ± 0.11
IRAS 19442	b	b	b	<2.78	<0.03	<2.81
IRAS 19598	<0.12	0.05 ± 0.02	<0.19	0.22 ± 0.04	0.21 ± 0.04	0.43 ± 0.08
DR21	<0.45	<0.10	<0.55	0.86 ± 0.17	0.10 ± 0.04	0.96 ± 0.22
IRAS 23133	0.39 ± 0.14	<0.06	0.39 ± 0.14	0.87 ± 0.17	<0.01	0.87 ± 0.17
Source	Sulphur ($\times 10^{-5}$)			Argon ($\times 10^{-6}$)		
	S ⁺⁺ /H	S ⁺³ /H	S/H	Ar ⁺ /H	Ar ⁺⁺ /H	Ar/H
IRAS 01045	0.10 ± 0.05	<0.19	<0.34	<0.29	<0.64	<0.93
IRAS 10589	0.78 ± 0.17	0.14 ± 0.07	0.92 ± 0.24	1.34 ± 0.16	1.71 ± 0.24	3.06 ± 0.40
IRAS 11143	0.75 ± 0.18	0.89 ± 0.36	1.64 ± 0.54	<0.11	1.92 ± 0.27	<2.30
IRAS 12063	0.29 ± 0.07	0.60 ± 0.29	0.89 ± 0.35	0.27 ± 0.04	1.82 ± 0.26	2.08 ± 0.29
IRAS 12073	0.26 ± 0.06	1.37 ± 0.68	1.64 ± 0.74	0.07 ± 0.03	1.75 ± 0.23	1.83 ± 0.26
IRAS 12331	0.91 ± 0.20	0.23 ± 0.10	1.14 ± 0.30	1.04 ± 0.16	3.10 ± 0.59	4.15 ± 0.75
IRAS 15384	0.53 ± 0.12	0.14 ± 0.06	0.66 ± 0.18	1.80 ± 0.23	1.86 ± 0.32	3.66 ± 0.55
IRAS 15502	0.14 ± 0.03	0.02 ± 0.01	0.15 ± 0.04	1.46 ± 0.21	0.78 ± 0.16	2.24 ± 0.37
IRAS 16128	0.20 ± 0.05 [†]	0.03 ± 0.01 [†]	0.24 ± 0.06 [†]	1.37 ± 0.12 [†]	0.62 ± 0.14 [†]	1.99 ± 0.25 [†]
IRAS 17160	0.22 ± 0.05	<0.03	0.22 ± 0.05	1.54 ± 0.22	0.86 ± 0.22	2.41 ± 0.43
IRAS 17221	0.64 ± 0.15	0.02 ± 0.01	0.66 ± 0.16	2.83 ± 0.34	1.27 ± 0.25	4.10 ± 0.59
IRAS 17279	0.67 ± 0.14	<0.03	0.67 ± 0.14	4.66 ± 0.63	0.82 ± 0.25	5.48 ± 0.88
IRAS 18032	0.76 ± 0.19	<0.01	0.76 ± 0.19	4.25 ± 0.57	0.77 ± 0.15	5.02 ± 0.72
IRAS 18479	0.17 ± 0.08	<0.19	<0.44	0.37 ± 0.05	<0.31	<0.73
IRAS 19442	0.42 ± 0.10	<0.06	<0.58	<6.66	<0.47	<7.17
IRAS 19598	0.10 ± 0.03	0.21 ± 0.12	0.31 ± 0.16	0.24 ± 0.03	0.66 ± 0.09	0.90 ± 0.12
DR21	0.20 ± 0.04	<0.01	0.20 ± 0.04	1.68 ± 0.25	0.40 ± 0.10	2.08 ± 0.35
IRAS 23133	0.48 ± 0.15	0.04 ± 0.02	0.51 ± 0.18	2.54 ± 0.31	0.70 ± 0.10	3.24 ± 0.40

◇ No LWS observation available. † No extinction was derived towards this source (see Table 6); consequently, this abundance is not corrected from extinction. ^b No [O III] density was calculated for this source (see Martín-Hernández et al. 2002a).

theoretical values. The aperture correction improves the agreement with the theoretical values considerably.

We want to point out that the “aperture” corrections applied above and in Sect. 5.2 may not be entirely appropriate for the VLA data. The VLA data is not sensitive to emission on scales larger than $\sim 20''$ (Wood & Churchwell 1989; Kurtz et al. 1994), which are of the order of the size of the SWS apertures. Hence, we could be missing part of the flux required for a proper correction.

5.4. The elemental abundance gradient

The sample analyzed here comprises 18 sources which span a large range in Galactocentric distance (~ 2 –14 kpc from the Galactic Center). A study of the variations of the elemental abundances with Galactocentric distance is thus possible. Moreover, we include 9 extra Galactic sources analyzed by Martín-Hernández et al. (2002a) once corrected for extinction and the Galactic T_e gradient. Following the indications given in Martín-Hernández et al. (2002a), we assume a T_e

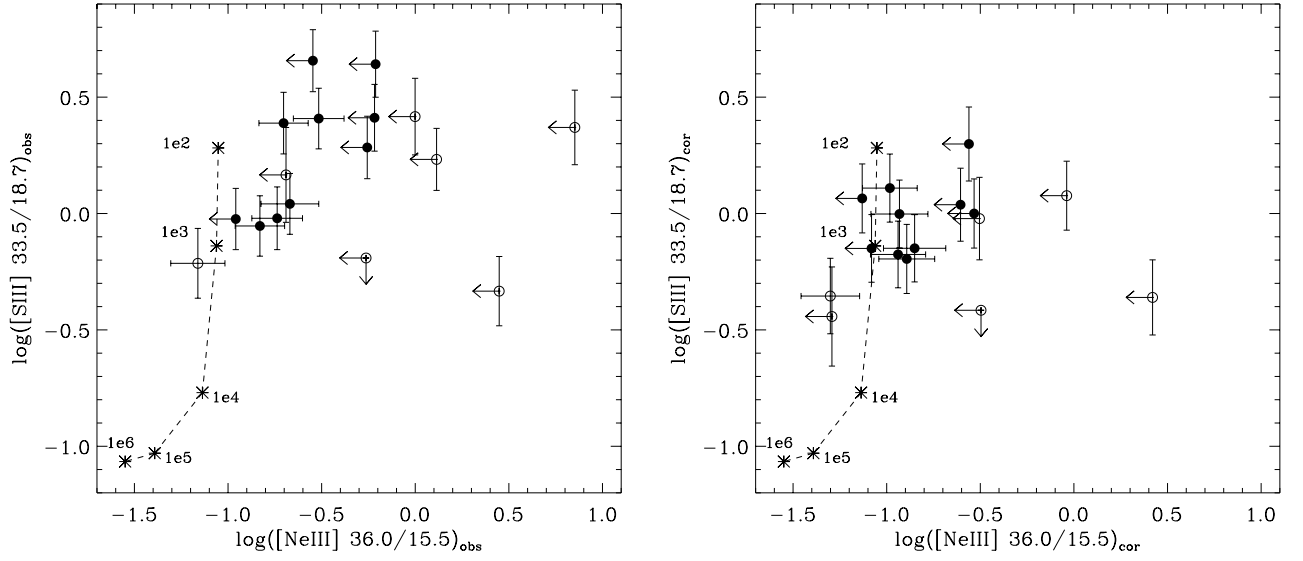


Fig. 11. *Left panel:* comparison between the observed [S III] 33/19 and [Ne III] 36/15 μm line ratios. *Right panel:* comparison between the extinguished and “aperture” corrected [S III] 33/19 and [Ne III] 36/15 μm line ratios. In both panels, the star symbols represent the theoretical values of both line ratios for electron densities 10^2 , 10^3 , 10^4 , 10^5 and 10^6 cm^{-3} . The ATCA sample is represented by filled circles and the VLA sample by open circles.

Table 9. Information on the extra nine Galactic sources taken from Martín-Hernández et al. (2002a) (see Sect. 5.4).

Source	R_{Gal} (kpc)	R (kpc)	A_K^\dagger	Ne/H ^b ($\times 10^{-4}$)	S/H ^b ($\times 10^{-5}$)	Ar/H ^b ($\times 10^{-6}$)	$\log N_{\text{Lyc}}^\ddagger$
IRAS 02219+6125	11.0	3.3	1.5 ± 0.5	1.4 ± 0.3	0.6 ± 0.2	2.6 ± 0.7	49.2
IRAS 17455–2800	0.2	8.3	1.8 ± 0.2	1.4 ± 0.3	0.9 ± 0.2	3.9 ± 0.5	48.7
IRAS 18116–1646	4.3	4.5	1.2 ± 0.3	1.9 ± 0.4	1.3 ± 0.3	6.8 ± 0.9	48.6
IRAS 18317–0757	4.5	4.9	2.0 ± 0.3	1.8 ± 0.4	0.9 ± 0.2	4.6 ± 0.7	48.2
IRAS 18434–0242	4.6	5.7	1.6 ± 0.2	1.8 ± 0.4	0.5 ± 0.1	4.0 ± 0.6	48.6
IRAS 18502+0051	4.7	7.1	2.2 ± 0.2	1.9 ± 0.4	0.7 ± 0.1	3.1 ± 0.4	48.5
IRAS 21190+5140	12.7	8.9	$<0.1^\ddagger$	1.0 ± 0.2	0.32 ± 0.05	1.9 ± 0.2	48.6
IRAS 22308+5812	11.3	5.5	$<0.1^\ddagger$	0.9 ± 0.2	0.5 ± 0.1	3.5 ± 0.7	48.0
IRAS 23030+5958	11.4	5.2	$<0.3^\ddagger$	1.5 ± 0.2	1.1 ± 0.2	3.0 ± 0.3	48.4

[†] K band extinction calculated from the $\text{Br}\beta/\text{Br}\alpha$ decrement. ^b Elemental abundance corrected for extinction and T_e variations. [‡] Lyman continuum flux from Martín-Hernández et al. (2002a). [¶] Taken as 0.

correction given by $T_e = 5000 + 5000 \times R_{\text{Gal}}/15$, with R_{Gal} in kpc. Table 9 shows the Galactocentric distances, K -band extinctions and corrected abundances of these extra 9 sources.

Figure 12 shows the elemental abundances determined in Sect. 5.3 as a function of the distance to the Galactic Center. The elemental abundances of all elements except for sulphur clearly decrease with Galactocentric distance. Least squares fits (represented by solid lines in Fig. 12) give:

$$\log(\text{Ne}/\text{H}) = (-3.53 \pm 0.04) - (0.051 \pm 0.005)R_{\text{Gal}},$$

$$\log(\text{Ar}/\text{H}) = (-5.12 \pm 0.03) - (0.048 \pm 0.004)R_{\text{Gal}},$$

$$\log(\text{S}/\text{H}) = (-4.97 \pm 0.07) - (0.027 \pm 0.009)R_{\text{Gal}} \text{ and}$$

$$\log(\text{N}/\text{H}) = (-3.39 \pm 0.14) - (0.098 \pm 0.017)R_{\text{Gal}}.$$

The gradients of Ne, Ar and N agree well with the elemental abundances of the Sun (Grevesse & Sauval 1998) and the Orion Nebula (Simpson et al. 1998). The slopes we find for Ne/H, Ar/H and S/H coincide well with those obtained by Giveon et al. (2002a); they reanalyze the elemental abundances presented in Martín-Hernández et al. (2002a) and in Giveon et al. (2002b) correcting for extinction (they adopt $A_{9.7}/A_K = 0.9$) and the Galactic T_e gradient. The slope found for N/H is in very good agreement with previous determinations based on KAO observations of H II regions (Simpson et al. 1995; Afflerbach et al. 1997; Rudolph et al. 1997). However, the slope we find here for S/H is considerably smaller than the one obtained in these KAO studies (~ 0.7 dex kpc^{-1}). Moreover, the sulphur abundances for $R_{\text{Gal}} < 8.5$ kpc are considerably lower than the solar and interstellar values.

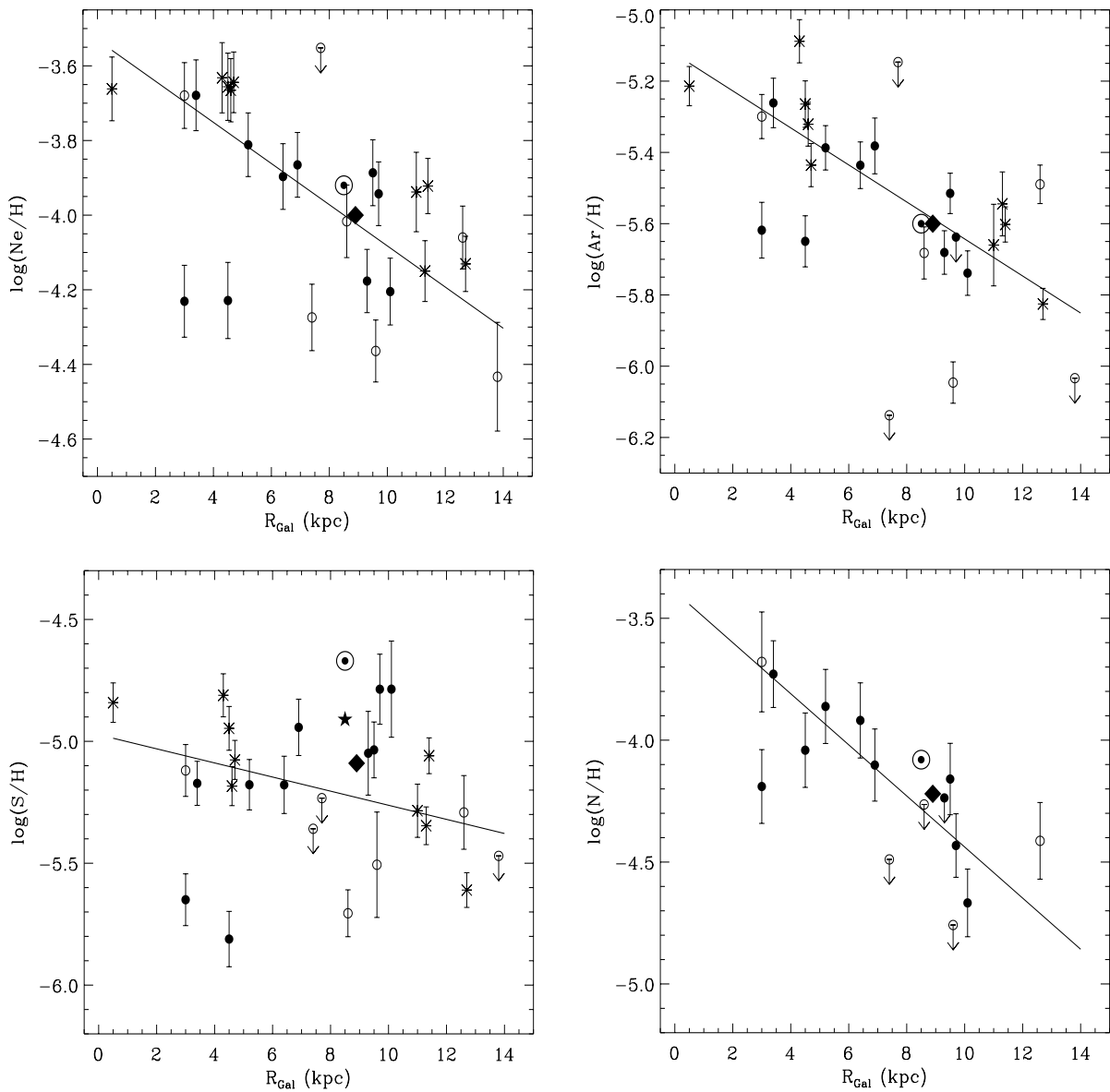


Fig. 12. Neon, argon, sulphur and nitrogen abundances of the sample sources as a function of the distance to the Galactic Center. The solar (Grevesse & Sauval 1998) and interstellar (Snow & Witt 1996) abundances are indicated by a \odot and a star symbol, respectively. Only for S/H, the difference between the solar and interstellar abundance is noticeable. The Orion abundances (Simpson et al. 1998; Esteban et al. 1998) are indicated by a filled diamond. The ATCA sample is represented by filled circles and the VLA sample by open circles. The elemental abundances adapted from Martín-Hernández et al. (2002a) are plotted as stars.

Two of the sources observed with the ATCA (IRAS 17160 and IRAS 15502) show especially low elemental abundances for their distances of 3 and 4.5 kpc from the Galactic Center. Because the nitrogen abundance calculated for IRAS 15502 is in reasonable agreement with those determined for the sample objects at a similar distance, we suppose that the extinction correction for the neon, sulphur and argon lines has been underestimated for this object. In fact, a $A_{9.7}/A_K < 2.2$ is determined from the [Ne III] line ratio for IRAS 15502 (cf. Sect. 5.2) and thus, the presence of an enhanced silicate feature is possible. For instance, for $A_{9.7}/A_K \sim 1$, the neon, sulphur and argon abundances would be approximately 2 times higher. In contrast, extinction seems not to be the cause for the general low

elemental abundance of IRAS 17160. First, N/H, which is not affected by extinction, is also substantially low. Second, we obtain that $A_{9.7}/A_K < 0.5$ for this source and thus, there is no evidence of enhanced silicate extinction.

The scatter shown by the sources observed by the VLA is larger than that presented by the ATCA sample by itself. The VLA observations (at 8.4 GHz) are made with a longer antenna spacing than the ATCA ones and therefore, any large scale structure ($>20''$) would be resolved out more easily. In terms of the elemental abundances, this has two opposite effects. As seen from Eq. (14), an underestimate of the flux density S_ν can produce too high an abundance. On the other hand, the extinction will also be underestimated, and this leads to

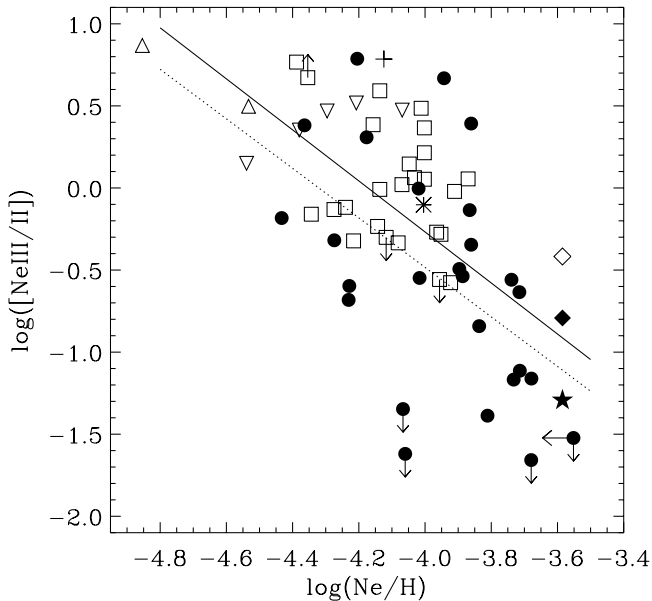


Fig. 13. Relation between the $[\text{Ne III}]/[\text{Ne II}]$ line ratio and the Ne/H elemental abundance for the combined sample of H II regions. Indicated by various symbols are the Galactic sample analyzed in this study, including the 9 sources adapted from Martín-Hernández et al. (2002a) (solid circles), Sgr A* (solid star), the Pistol (open diamond), the Sickle (solid diamond), the Orion nebula (star), the M 33 sample (open squares), the LMC sample (reverse open triangles, except 30 Dor, which is plotted as a plus sign) and 2 regions in the SMC (open triangles). The solid line is a least squares fit to the whole data. The dotted line is a least-squares fit to the Galactic sample only.

an underestimate of the elemental abundances. The generally lower abundances of the VLA sample indicate that the latter effect is probably the dominant one.

5.5. Stellar luminosity, metallicity and nebular ionization structure

The present study allows us to examine directly the interplay between the stellar luminosity, metallicity and the ionization structure of the nebulae.

5.5.1. Degree of ionization and metallicity

The ionization structure of the nebula can be traced by the ratio of successive stages of ionization X^{+i} and $X^{+(i+1)}$ of a given element. Basically, such a ratio depends, for a given ionization parameter U , on the number of photons able to ionize X^{+i} compared to the number of Lyman continuum photons (Vilchez & Pagel 1988). Four different ionization tracers are available from the ISO spectra: $[\text{N III}]/[\text{N II}]$ 57.3/121.7, $[\text{Ar III}]/[\text{Ar II}]$ 9.0/7.0, $[\text{S IV}]/[\text{S III}]$ 10.5/18.7 and $[\text{Ne III}]/[\text{Ne II}]$ 15.5/12.8 μm . In Martín-Hernández et al. (2002a) it was shown that all these tracers correlate well with each other. We chose to use the $[\text{Ne III}]/[\text{Ne II}]$ line ratio. This ratio is not very sensitive to systematic errors because the lines involved have been observed with the same ISO-SWS band 3A aperture.

Finally, we chose to use Ne/H as a tracer of the nebular metallicity. As a primary element, the abundance of neon follows that of oxygen (Henry & Worthey 1999).

In Martín-Hernández et al. (2002b), we compare the degree of ionization of the ionized gas within the nebula, as traced by the $[\text{Ne III}]/[\text{Ne II}]$ line ratio, with the nebular Ne/H metallicity. The sample comprised a large number of Galactic (which included a large fraction of the sources considered here) and Magellanic Cloud H II regions. It was found that metallicity strongly influences the observed $[\text{Ne III}]/[\text{Ne II}]$ line ratio and therefore, the characteristics of the ionizing star as derived from this ratio. Willner & Nelson-Patel (2002) have recently presented an analysis of 25 H II regions in M 33 based on ISO-SWS observations. They measured the $[\text{Ne II}]$ 12.8 and $[\text{Ne III}]$ 15.5 μm line fluxes and derived Ne/H abundances. We can further study here this correlation between metallicity and ionization structure with the inclusion of this large dataset of extragalactic H II regions, for which no selection effect in terms of distance exists.

Figure 13 shows the plot of $[\text{Ne III}]/[\text{Ne II}]$ against Ne/H . Together with the Galactic H II region sample presented in this study, we include the Orion nebula and 3 sources in the Galactic Center: Sgr A* and the Sickle and Pistol H II regions. An infrared spectrum integrated over the whole Orion nebula was obtained by Simpson et al. (1998) using the MSX satellite. They measure both the $[\text{Ne II}]$ and $[\text{Ne III}]$ line fluxes and derive Ne/H . The Galactic Center sources have been observed by ISO-SWS. The SWS spectrum of Sgr A* has been analyzed by Lutz et al. (1996), who listed, together with the fine-structure line fluxes, the fluxes of H I recombination lines. We calculate Ne/H from the $[\text{Ne II}]$, $[\text{Ne III}]$ and $\text{Br}\alpha$ lines assuming an electron temperature of 5000 K, characteristic of H II regions in the Galactic Center (Shaver et al. 1983; Afflerbach et al. 1996, 1997; Deharveng et al. 2000), the low density limit and a visible extinction of 31 magnitudes (Rieke et al. 1989). We obtain $\text{Ne}/\text{H} \sim 2.6 \times 10^{-4}$. $[\text{Ne II}]$ and $[\text{Ne III}]$ line fluxes are reported in the Sickle and Pistol H II regions by Rodríguez-Fernández et al. (2001). We consider that these two H II regions have a Ne/H abundance equal to the abundance we calculate for Sgr A*. Among the extragalactic H II regions, we include the sample in M 33 and the H II regions in the Large and Small Magellanic Clouds presented and analyzed by Vermeij et al. (2002a) and Vermeij & van der Hulst (2002). The neon abundances listed by Willner & Nelson-Patel (2002) were calculated assuming an electron temperature of 10^4 K. We have scaled these abundances to $T_e = 7500$ K, which is the electron temperature we have used throughout this study.

Figure 13 shows that a clear correlation exists between $[\text{Ne III}]/[\text{Ne II}]$ and Ne/H , albeit with a large scatter (approximately 1.5 dex in $\log([\text{Ne III}]/[\text{Ne II}])$ for a given Ne/H). This scatter is probably real and due to variations in the stellar effective temperature (see Martín-Hernández et al. 2002b). The extragalactic sample perfectly overlaps the parameter space determined by the Galactic sample. The least squares fits to the whole dataset and to only the Galactic sample yield the same slopes: -1.5 ± 0.2 and -1.5 ± 0.5 , respectively. This figure confirms our previous conclusion in Martín-Hernández et al. (2002b) that the increase in degree of ionization of the H II

regions is a direct consequence of the hardening of the stellar radiation due to the decreased metallicity.

5.5.2. Luminosity and metallicity

We can now examine if the number of stellar Lyman ionizing photons, $N_{\text{Ly}\alpha}$, is somewhat modified by changes in metallicity.

The comparison of the $N_{\text{Ly}\alpha}$ value determined in Sect. 4 from the integrated radio flux with the properties (such as the Ne/H elemental abundance) obtained from the ISO data requires a detailed look at the source morphology. For most of the objects, the number of ionizing photons required to ionize the whole nebula is suitable for the comparison. In the case of objects with separate components, we only consider the number of photons necessary to ionize the component included in the ISO beam. In this sense, only the Lyman continuum flux determined for IRAS 12073 A, IRAS 17160 A, IRAS 17279 A and IRAS 18032 B is used in the comparison with the elemental abundance of the respective IRAS sources. In the cases of IRAS 15502 and DR 21, the added contribution of components A and B is considered as they are both included in the ISO beam.

The Lyman ionizing photon fluxes of the extra nine Galactic sources taken from Martín-Hernández et al. (2002a) are given in Table 9. The total $N_{\text{Ly}\alpha}$ of the Pistol and Sickie H II regions is taken from Lang et al. (1997). We calculate the Lyman photon rate for Sgr A* from the total flux density at 4.8 GHz given by Falcke et al. (1998) and assuming $T_e = 5000$ K. In the case of the Orion nebula, the single dish radio flux at 24 GHz given by Chaisson & Dopita (1977) is used assuming $T_e = 7500$ K. The total $N_{\text{Ly}\alpha}$ of 30 Dor is taken from Peck et al. (1997). The $N_{\text{Ly}\alpha}$ values of the other Magellanic Cloud H II regions are taken from new ATCA 4.8 GHz measurements by R. Vermeij (private communication). Finally, we calculate the Lyman photon rate of the M 33 H II regions using the 5 GHz flux densities given by Willner & Nelson-Patel (2002) and assuming $T_e = 7500$ K.

Figure 14 shows the relation between Ne/H and the stellar $N_{\text{Ly}\alpha}$. If one just considers the Galactic sample (solid circles), it seems that indeed there is a correlation between the stellar UV flux and the metallicity in the sense that as $N_{\text{Ly}\alpha}$ increases, the metallicity decreases. The least squares fit gives a slope of -0.16 ± 0.06 . The inclusion of the Galactic Center sources and the extragalactic H II regions significantly flattens the trends. In this case, the slope is -0.10 ± 0.03 . It is interesting to note that the M 33 sample is restricted to rather high values of $N_{\text{Ly}\alpha}$ ($10^{49.5}$ – 10^{51} photons s^{-1}), which correspond to typical values of large, classical H II regions (cf. Sect. 4). However, the spread in metallicity (M 33 has a significant abundance gradient) is rather large. 30 Doradus, with $N_{\text{Ly}\alpha} \sim 10^{52}$ photons s^{-1} , is a giant H II region with a linear diameter of ~ 400 pc and is powered by the R136 cluster, which is a very massive site of recent star formation with approximately 1000 ionizing O stars. We expect that similar giant H II regions and nuclear starbursts in galaxies will span a similar range in metallicity as the M 33 sample but at larger values of $N_{\text{Ly}\alpha}$ (10^{52} – 10^{54} photons s^{-1}) and therefore, will flatten this trend even more.

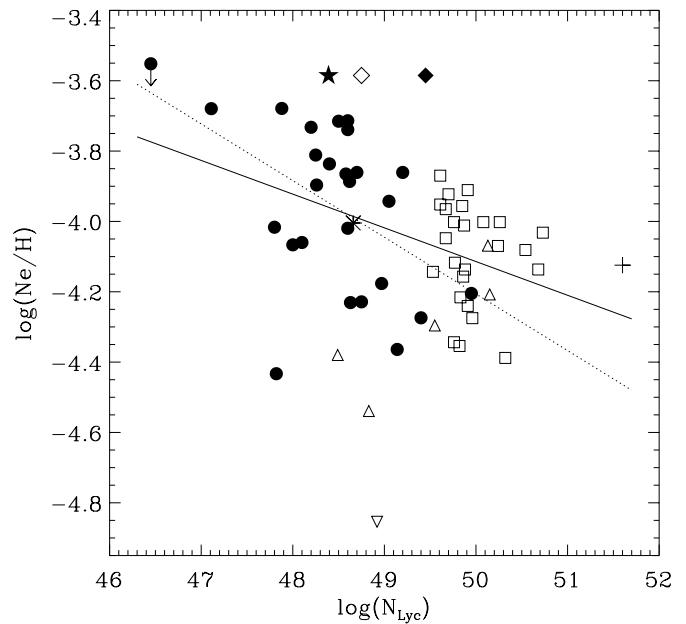


Fig. 14. The [Ne III]/[Ne II] line ratio is plotted against $N_{\text{Ly}\alpha}$. The description of symbols and lines is given in Fig. 13.

Recently, several authors (e.g. Giveon et al. 2002b; Smith et al. 2002; Martín-Hernández et al. in prep) have investigated the effect of metallicity on the stellar spectral energy distribution of O stars using state-of-the-art stellar atmosphere models. They find that the total number of Lyman photons emitted by the star is independent of line blanketing effects and metallicity for a given effective temperature. The fact that we do not observe a clear trend of $N_{\text{Ly}\alpha}$ with metallicity (Fig. 14) supports this theoretical result.

6. Summary and conclusions

We report ATCA observations at 4.8 and 8.6 GHz of 11 southern H II regions. These sources form part of the ISO spectral catalogue of H II regions presented in Peeters et al. (2002b). The objectives were to determine the morphologies and physical properties of the ionized gas, by using the radio fluxes by themselves or in combination with the ISO observations, and to constrain the characteristics of their ionizing stars. The main results and conclusions are as follows:

- Nine of the total sample of 11 IRAS sources observed turned out to have multiple components. In total, we have detected 19 individual regions. We identify 3 cometary, 2 core-halo, 6 spherical or unresolved and 8 complex sources with multiple embedded components. The linear diameters of these regions range from 0.03 pc to 3 pc, the electron densities from 300 to $2.5 \times 10^4 \text{ cm}^{-3}$ and the number of Lyman continuum photons from 10^{47} to 10^{50} s^{-1} . The relation between the electron density and the physical diameter can be fit by a power-law which agrees with that found by Garay et al. (1993): $n_e \propto D^{-1}$. This power-law is flatter than expected for a pure hydrogen Strömgen sphere. Several hypothesis that could make this n_e - D

relation shallower are discussed in detail. However, no definitive conclusion could be drawn on the basis of the present data.

- A puzzling East-West linear feature has been detected on the West side of IRAS 15384–5348. This filament is 55'' in length and 15'' in width. Five knots can be distinguished along the filament. This knot structure is highly symmetric with respect to the center knot. The *SuperCOSMOS Sky Survey* image in the *I*-band reveals no clear counterpart. The comparison with the infrared MSX images shows, on the other hand, a structure that could be identified with the feature, hence pointing towards a Galactic origin for the filament. The nature of this feature is, however, unclear. Follow-up observations are needed to clarify it.
- We have conducted a detailed analysis of the radio images in order to determine the total radio flux density associated to the different ISO apertures. This has allowed us a proper comparison with the ISO data. In this analysis, we included 7 “northern” sources previously observed by the VLA. Based on the combined radio and infrared study, we have derived estimates of the extinction in the infrared and calculated the elemental abundances of nitrogen, neon, argon and sulphur.
- Values for the extinction in the *K*-band between ~ 0 and 6 magnitudes are found. The data seems to agree well with a non-enhanced silicate feature, i.e. $A_{9.7}/A_K = 0.5$.
- The derived elemental abundances are found to decrease with Galactocentric distance. The gradients we find are: $\Delta \log(\text{Ne}/\text{H}) = -0.053 \pm 0.005$, $\Delta \log(\text{Ar}/\text{H}) = -0.050 \pm 0.004$, $\Delta \log(\text{N}/\text{H}) = -0.11 \pm 0.02$ and $\Delta \log(\text{S}/\text{H}) = -0.027 \pm 0.009 \text{ dex kpc}^{-1}$.
- We have studied the correlation between degree of ionization (traced by the mid-infrared $[\text{Ne III}] 15.5/[\text{Ne III}] 12.8 \mu\text{m}$ line ratio) and metallicity (from Ne/H) with the inclusion of the H II region sample in M 33 analyzed by Willner & Nelson-Patel (2002), the Magellanic Cloud sample by Vermeij et al. (2002a), the Orion nebula and 3 sources located in the Galactic Center: SgrA*, the Pistol and the Sickle. The least squares fit to the whole dataset gives a significant slope of -1.5 ± 0.2 , albeit with a large scatter. This scatter is probably real and due to variations in the stellar effective temperature. We have further studied whether metallicity could have some influence on the number of Lyman photons. We did not find, however, in agreement with theoretical results, a clear trend of $N_{\text{Ly}\alpha}$ with metallicity.

Acknowledgements. We wish to thank the referee, R. Cesaroni, whose comments greatly improved this article. We also thank E. Churchwell for making the VLA images of ultracompact H II regions available to us. NLMH thanks specially M. E. Filho and H. R. Klöckner for their useful pieces of advice concerning the radio data reduction.

References

Afflerbach, A., Churchwell, E., Acord, J. M., et al. 1996, *ApJS*, 106, 423

- Afflerbach, A., Churchwell, E., & Werner, M. W. 1997, *ApJ*, 478, 190
 Becker, R. H., White, R. L., Helfand, D. J., & Zoonematkermani, S. 1994, *ApJS*, 91, 347
 Boogert, A. C. A. 1999, Ph.D. Thesis
 Caswell, J. L., & Haynes, R. F. 1987, *A&A*, 171, 261
 Chaisson, E. J., & Dopita, M. A. 1977, *A&A*, 56, 385
 Chini, R., Kruegel, E., & Kreysa, E. 1986, *A&A*, 167, 315
 Churchwell, E., Wolfire, M. G., & Wood, D. O. S. 1990, *ApJ*, 354, 247
 Copetti, M. V. F., Mallmann, J. A. H., Schmidt, A. A., & Castañeda, H. O. 2000, *A&A*, 357, 621
 Deharveng, L., Peña, M., Caplan, J., & Costero, R. 2000, *MNRAS*, 311, 329
 Draine, B. T. 1985, *ApJS*, 57, 587
 Draine, B. T. 1989, in *Infrared Spectroscopy in Astronomy*, ESA SP-290, 93–98
 Draine, B. T., & Lee, H. M. 1984, *ApJ*, 285, 89
 Draine, B. T., & Salpeter, E. E. 1979, *ApJ*, 231, 438
 Esteban, C., Peimbert, M., Torres-Peimbert, S., & Escalante, V. 1998, *MNRAS*, 295, 401
 Faison, M., Churchwell, E., Hofner, P., et al. 1998, *ApJ*, 500, 280
 Falcke, H., Goss, W. M., Matsuo, H., et al. 1998, *ApJ*, 499, 731
 Fich, M. 1993, *ApJS*, 86, 475
 Garay, G., & Lizano, S. 1999, *PASP*, 111, 1049
 Garay, G., Rodríguez, L. F., Moran, J. M., & Churchwell, E. 1993, *ApJ*, 418, 368
 Giveon, U., Morisset, C., & Sternberg, A. 2002a, *A&A*, 392, 501
 Giveon, U., Sternberg, A., Lutz, D., Feuchtgruber, H., & Pauldrach, A. W. A. 2002b, *ApJ*, 566, 880
 Grevesse, N., & Sauval, A. J. 1998, *Space Sci. Rev.*, 85, 161
 Henry, R. B. C., & Worthey, G. 1999, *PASP*, 111, 919
 Hummer, D. G., & Storey, P. J. 1987, *MNRAS*, 224, 801
 Kim, K., & Koo, B. 2001, *ApJ*, 549, 979
 Kurtz, S., Churchwell, E., & Wood, D. O. S. 1994, *ApJS*, 91, 659
 Kurtz, S. E., Watson, A. M., Hofner, P., & Otte, B. 1999, *ApJ*, 514, 232
 Lang, C. C., Goss, W. M., & Wood, D. O. S. 1997, *ApJ*, 474, 275
 Lutz, D., Feuchtgruber, H., Genzel, R., et al. 1996, *A&A*, 315, L269
 Martin, P. G., & Whittet, D. C. B. 1990, *ApJ*, 357, 113
 Martín-Hernández, N. L., Peeters, E., Morisset, C., et al. 2002a, *A&A*, 381, 606
 Martín-Hernández, N. L., Vermeij, R., Tielens, van der Hulst, J. M., & Peeters, E. 2002b, *A&A*, 389, 286
 Mathis, J. S. 1990, *ARA&A*, 28, 37
 McLaughlin, B. M., & Bell, K. L. 2000, *J. Phys. B*, 33, 597
 Mezger, P. G., & Henderson, A. P. 1967, *ApJ*, 147, 471
 Milne, D. K., & Aller, L. H. 1982, *A&AS*, 50, 209
 Natta, A., & Panagia, N. 1976, *A&A*, 50, 191
 Osterbrock, D. E. 1989, *Astrophysics of gaseous nebulae and active galactic nuclei* (Research supported by the University of California, John Simon Guggenheim Memorial Foundation, University of Minnesota, et al. (Mill Valley, CA, University Science Books)
 Peck, A. B., Goss, W. M., Dickel, H. R., et al. 1997, *ApJ*, 486, 329
 Peeters, E., Hony, S., Van Kerckhoven, C., et al. 2002a, *A&A*, 390, 1089
 Peeters, E., Martín-Hernández, N. L., Damour, F., et al. 2002b, *A&A*, 381, 571
 Persson, S. E., & Campbell, B. 1987, *AJ*, 94, 416
 Petrosian, V., Silk, J., & Field, G. B. 1972, *ApJ*, 177, L69
 Rieke, G. H., & Lebofsky, M. J. 1985, *ApJ*, 288, 618
 Rieke, G. H., Rieke, M. J., & Paul, A. E. 1989, *ApJ*, 336, 752
 Roche, P. F., & Aitken, D. K. 1984, *MNRAS*, 208, 481
 Roche, P. F., & Aitken, D. K. 1985, *MNRAS*, 215, 425

- Rodríguez-Fernández, N. J., Martín-Pintado, J., & de Vicente, P. 2001, *A&A*, 377, 631
- Rudolph, A. L., Brand, J., de Geus, E. J., & Wouterloot, J. G. A. 1996, *ApJ*, 458, 653
- Rudolph, A. L., Simpson, J. P., Haas, M. R., Erickson, E. F., & Fich, M. 1997, *ApJ*, 489, 94
- Russeil, D. 1997, *A&A*, 319, 788
- Salama, A. 2000, *ISO Beyond Point Sources: Studies of Extended Infrared Emission*, September 14-17, 1999, ISO Data Centre, Villafranca del Castillo, Madrid, Spain, ed. R. J. Laureijs, K. Leech, & M. F. Kessler, ESA-SP 455, 7
- Sault, R. J., Teuben, P. J., & Wright, M. C. H. 1995, in *ASP Conf. Ser. 77: Astronomical Data Analysis Software and Systems IV*, 4, 433
- Shaver, P. A., McGee, R. X., Newton, L. M., Danks, A. C., & Pottasch, S. R. 1983, *MNRAS*, 204, 53
- Simpson, J. P., Colgan, S. W. J., Rubin, R. H., Erickson, E. F., & Haas, M. R. 1995, *ApJ*, 444, 721
- Simpson, J. P., & Rubin, R. H. 1990, *ApJ*, 354, 165
- Simpson, J. P., Witteborn, F. C., Price, S. D., & Cohen, M. 1998, *ApJ*, 508, 268
- Smith, L. J., Norris, R. P. F., & Crowther, P. A. 2002, *MNRAS*, 337, 1309
- Snow, T. P., & Witt, A. N. 1996, *ApJ*, 468, L65
- Steer, D. G., Dewdney, P. E., & Ito, M. R. 1984, *A&A*, 137, 159
- Storey, P. J., & Hummer, D. G. 1995, *MNRAS*, 272, 41
- Tielens, A. G. G. M., & de Jong, T. 1979, *A&A*, 75, 326
- Vacca, W. D., Garmany, C. D., & Shull, J. M. 1996, *ApJ*, 460, 914
- Vermeij, R., Damour, F., van der Hulst, J. M., & Baluteau, J.-P. 2002a, *A&A*, 390, 649
- Vermeij, R., Peeters, E., Tielens, A. G. G. M., & van der Hulst, J. M. 2002b, *A&A*, 382, 1042
- Vermeij, R., & van der Hulst, J. M. 2002, *A&A*, 391, 1081
- Vílchez, J. M., & Pagel, B. E. J. 1988, *MNRAS*, 231, 257
- Weingartner, J. C., & Draine, B. T. 2001, *ApJ*, 548, 296
- Willner, S. P., & Nelson-Patel, K. 2002, *ApJ*, 568, 679
- Wood, D. O. S., & Churchwell, E. 1989, *ApJS*, 69, 831